Geochemistry 86 (2026) 126388

Contents lists available at ScienceDirect

Geochemistry

journal homepage: www.elsevier.com/locate/chemer

Unravelling the origin of A-type granites in an extensional arc setting: Insights from the Permian El Fierro pluton, Colangüil batholith (Frontal Cordillera, Argentina)

Juan A. Moreno[a,b,*], Gilmara Santos da Cruz[c,d], Juan A. Dahlquist[c,d], Matías M. Morales Cámera[c,d], Priscila S. Zandomeni[d], Gabriela A. Gonzalez-Liedtke[c,d], Miguel A.S. Basei[e], Sanjeet K. Verma[f]

[a] *Department of Earth Sciences - Faculty of Experimental Sciences, University of Huelva, 21071, Huelva, Spain*
[b] *Center for Research in Sustainable Chemistry (CIQSO), University of Huelva, 21071, Huelva, Spain*
[c] *Centro de Investigaciones en Ciencias de la Tierra, Consejo Nacional de Investigaciones Científicas y Técnicas, Av. Vélez Sársfield 1611, Ciudad Universitaria, X5016GCA, Córdoba, Argentina*
[d] *Facultad de Ciencias Exactas, Físicas y Naturales, Universidad Nacional de Córdoba, Av. Vélez Sársfield 1611, Ciudad Universitaria, X5016GCA, Córdoba, Argentina*
[e] *Instituto de Geociências, Universidade de São Paulo, do lago 562 - Butantã, São Paulo, SP, 05508-080, Brazil*
[f] *División de Geociencias Aplicadas, Instituto Potosino de Investigación Científica y Tecnológica (IPICYT), Camino a la Presa San José 2055, 78216, San Luis Potosí, Mexico*

ARTICLE INFO

Handling Editor: Astrid Holzheid

Keywords:
High F A-type granites
Choiyoi Magmatic Province
Granite petrogenesis
Metasomatized continental crust
Extensional arc regime

ABSTRACT

The El Fierro pluton represents one of the late-stage plutons of the Choiyoi Magmatic Province in the Colangüil batholith (Frontal Cordillera, Argentina). New U-Pb zircon dating yields a crystallisation age of 262 ± 2 Ma, with zircon antecrysts (~273 Ma) indicating prolonged magmatic activity that overlaps with the early-stage Choiyoi I-type magmatism (ca. 270–290 Ma). This pluton is ferroan, alkali-calcic to calc-alkalic, and essentially weakly peraluminous (av. 1.05 ± 0.06), exhibiting high Ga/Al ratios, elevated HFSE concentrations (Ce + Zr + Nb + Y; av. 310 ± 147 ppm; range: 150–584 ppm), extreme F enrichment (6101–31,442 ppm) and relatively high zircon-saturation (775 ± 45 °C) and apatite-saturation temperatures (887 ± 78 °C), consistent with an A-type affinity. Isotope data ($\varepsilon Hf_t = -7.0$ to $+1.25$; $\varepsilon Nd_i \approx -3$), together with geochemical compositions, reflect a hybrid crustal source involving metasedimentary components likely metasomatized by mantle fluids. Accordingly, we interpret the El Fierro pluton as the product of crustal melting during lithospheric thinning and slab retreat, marking the onset of incipient rifting in southwestern Gondwana. This study highlights that A-type granites can be generated in extensional regimes within arc settings.

1. Introduction

The Carboniferous to Triassic magmatism along the pre-Andean margin of southwestern Gondwana (25°–40°S) has been the subject of numerous studies (e.g., del Rey et al., 2016; Rocher et al., 2015, 2024; Sato et al., 2015; Moreno et al., 2020; Oliveros et al., 2020; Dahlquist et al., 2018, 2021; Gianni and Navarrete, 2022; Santos da Cruz et al., 2024, and references therein). A consensus supports the persistence of subduction-related magmatism during this interval, with temporal and spatial variations linked to changes in the subduction geometry and the prevailing tectonic regime–ranging from compressional to extensional. Notably, Moreno et al. (2020) identified a trench-ward migration of Carboniferous arc magmatism, whereas Dahlquist et al. (2021) reported a magmatic gap between the Carboniferous and Permian-Triassic periods in Argentina, a hiatus not observed in Chile (Oliveros et al., 2020).

The Permian–Triassic magmatism is best represented by the Choiyoi Magmatic Province (Fig. 1A), one of the most voluminous and long-lived magmatic events in southwestern Gondwana (846,545 km^2; Rocher et al., 2015, 2024; Dahlquist et al., 2024a). This province comprises widespread volcanic and plutonic rocks emplaced in a subduction-related magmatic context with progressive tectonic extension. Early phases are dominated by voluminous calc-alkaline and transitional I-

---

* Corresponding author at: Department of Earth Sciences - Faculty of Experimental Sciences, University of Huelva, 21071 Huelva. Spain.
E-mail address: juanantonio.moreno@dct.uhu.es (J.A. Moreno).

https://doi.org/10.1016/j.chemer.2026.126388
Received 3 October 2025; Received in revised form 9 January 2026; Accepted 10 January 2026

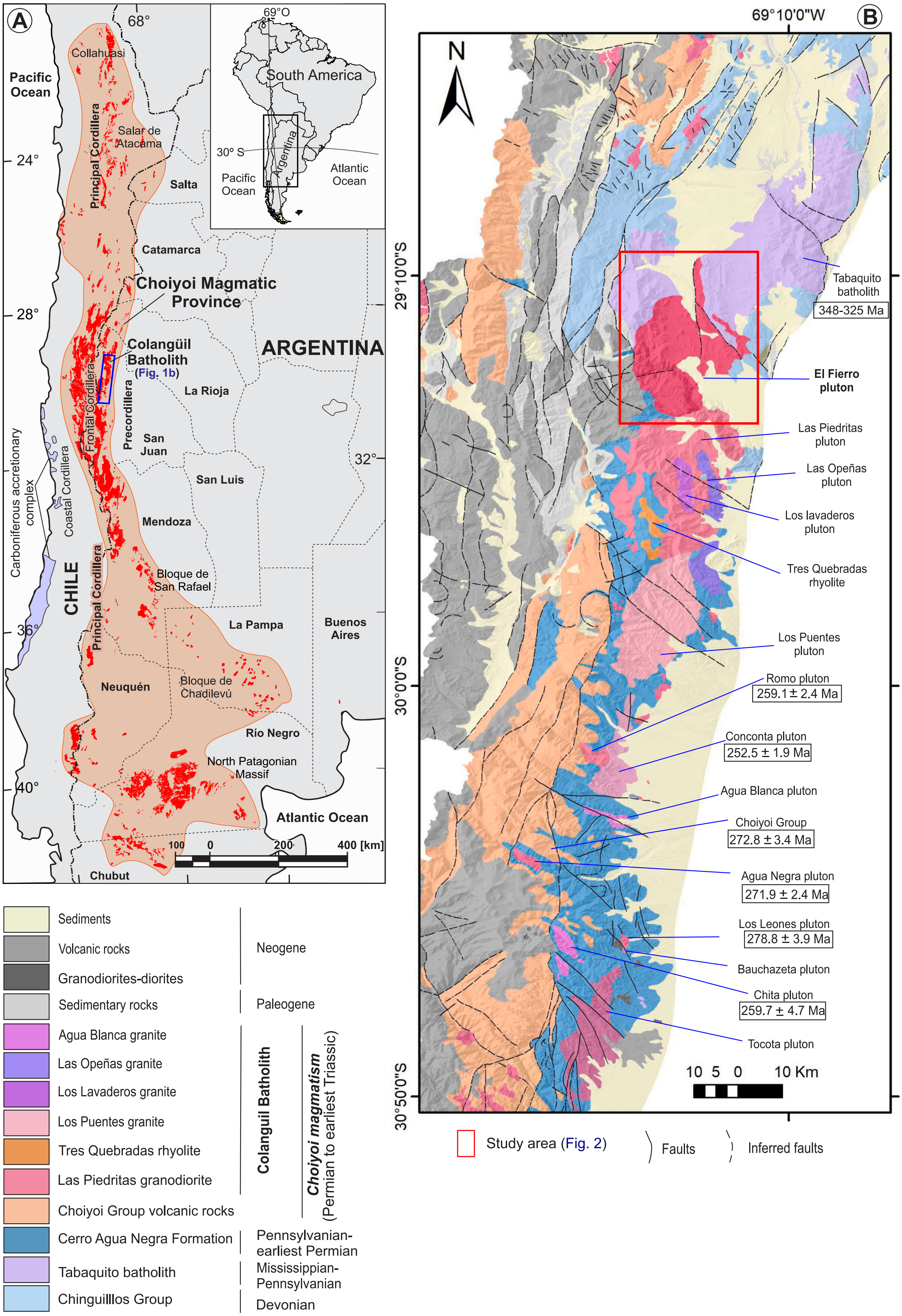

Fig. 1. Regional geological setting of the Choiyoi Magmatic Province and the Colangüil batholith. A) Location of the Choiyoi Magmatic Province in southwestern Gondwana, highlighting the position of the Colangüil batholith (modified from Rocher et al., 2015). B) Simplified geological map of the Colangüil batholith showing the location of the El Fierro pluton. Modified from Cardó et al. (2005, 2007) and Sato et al. (2015).

type magmatism, whereas the later stages—particularly during the Late Permian—display a shift toward more evolved and alkaline compositions, including rocks with A-type geochemical affinities (e.g., Llambías and Sato, 1995; Sato et al., 2015; Rocher et al., 2015, 2024; Dahlquist et al., 2024a). Considering the available geochronology of plutonic rocks of the Choiyoi group, Rocher et al. (2024) differentiated the early-stage plutons of calc-alkaline I-type affinity (ca. 285–272 Ma) and the late-stage plutons with a variable A-type signature (ca. 265–252 Ma) in the Argentine Frontal Cordillera. Conversely, a younger magmatism at ca. 241 Ma, is mainly recorded in Chile.

Plutonic counterparts of this magmatism are well exposed in the Frontal Cordillera of Argentina, particularly in the Colangüil batholith. This intrusive complex was originally described by Llambías and Sato (1995), who recognized multiple plutons emplaced during the Permian-Triassic. Subsequent studies (e.g., Sato et al., 2015) indicate a magmatic evolution from early calc-alkaline I-type intrusions (~280 Ma) to younger A-type granites (<~265 Ma). This transition is also mirrored in the volcanic sequences of the Choiyoi Group (Llambías and Sato, 1995; Rocher et al., 2015, 2024).

Although A-type granites are commonly reported in foreland or retro-arc regions (e.g., Dahlquist et al., 2021), our study is of significant relevance as it provides new constraints on the generation of A-type magmatism (El Fierro pluton) within a Cordilleran batholith (Colangüil batholith).This study integrates fieldwork with petrographic, geochemical, geochronological, and isotopic data to better understand the origin and significance of this granitic magmatism within the late stages of the Choiyoi Magmatic Province. In addition, this study also seeks to contribute to understanding the generation of A-type granites and their enrichment in HFSE, which are currently of great economic interest.

2. Geological setting

2.1. The Argentine Frontal Cordillera and the Colangüil batholith

The Frontal Cordillera of Argentina (Fig. 1A) is a morphostructural province located west of the Precordillera, extending from ~27°S to ~34°S (Caminos, 1979). It comprises three main geological domains (Sato et al., 2015; Dahlquist et al., 2021 and references therein): (1) a pre-Carboniferous basement of Ediacaran–Cambrian low- to medium-grade metasedimentary and metavolcanic rocks affected by Devonian metamorphism, and Ordovician to Devonian sedimentary sequences (e.g., Chinguillos and Ciénaga del Medio groups) intruded by Devonian granitoids to south 34°S; (2) Carboniferous to Triassic volcanic and plutonic rocks linked to the Gondwanide orogeny, including the Cerro Agua Negra Formation, the Choiyoi Group, and the Tabaquito and Colangüil batholiths; and (3) Jurassic to Neogene units related to the Andean orogeny.

During the Permian–Triassic, igneous activity occurred in an arc setting under extensional conditions, marking the final stages of subduction along the southwestern Gondwanan margin (Kay et al., 1989; Llambías and Sato, 1995; Rocher et al., 2024). This tectonomagmatic setting favoured the emplacement of large Permian granitoid batholiths, such as the Colangüil and El Portillo batholiths (Kay et al., 1989; Llambías and Sato, 1990; Azcuy et al., 1999; Dahlquist et al., 2024a; Rocher et al., 2024).

The Colangüil batholith (Fig. 1B), named by Quartino and Zardini (1967) after Groeber's (1951) earlier descriptions, is located between ~29°S and ~ 31°S to the north of the San Juan Province. It spans ~1500 km^2 and mainly intrudes Pennsylvanian to earliest Permian marine siliciclastic sedimentary rocks of the Cerro Agua Negra Formation (Llambías and Sato, 1990, 1995; Sato et al., 2015; Rocher et al., 2024). It consists mostly of leucocratic granodiorites and granites with U-Pb zircon ages between 280 and 252 Ma (e.g., Llambías and Sato, 1995; Sato et al., 2015; Jones et al., 2015; Poole et al., 2020), as well as minor subvolcanic rhyolites.

The batholith comprises several plutonic units with distinct ages and petrological characteristics (Llambías and Sato, 1990, 1995; Sato et al., 2015). The main units (Fig. 1B) include:

- *Las Piedritas Granodiorite* comprises the Los Leones, Agua Negra, Tocota, Romo, and Las Piedritas plutons. These medium- to coarse-grained I-type granitoids range from granodiorite to tonalite and exhibit calc-alkaline affinities. Reported crystallisation ages are: 279 ± 4 Ma (Los Leones pluton), 272 ± 2 Ma (Agua Negra pluton) and 259 ± 2 Ma (Romo pluton) from LA-MC-ICP-MS U-Pb zircon dating; 269–267 Ma (Tocota pluton) and 262–253 Ma (Las Piedritas pluton) from Rb-Sr whole-rock–biotite isochrons (Llambías and Sato, 1995; Sato et al., 2015; Jones et al., 2015; Poole et al., 2020).
- *Los Puentes Granite,* composed of the El Fierro (focus of this study), Los Puentes, and Conconta plutons, represents nearly half of the Permian granitoids in the batholith. These are gray, massive, equigranular granites mainly formed of K-feldspar, plagioclase, quartz, and biotite, with fine-grained leucocratic facies displaying miarolitic cavities and aplitic to pegmatitic segregations. Although coarse-grained porphyritic facies and fine-grained leucocratic facies have also been described (Moreno et al., 2020), see more details below. Reported ages for the Los Puentes Granite indicate an emplacement age of ca. 257 ± 1 Ma, based on Rb-Sr whole-rock–biotite isochron dating of the El Fierro and Los Puentes plutons (Llambías and Sato, 1995). A younger U-Pb zircon age of 253 ± 2 Ma, obtained for the Conconta pluton (Sato et al., 2015), has been preliminarily considered as representative of the age of the Los Puentes Granite.
- *Los Lavaderos Granite* is a 39 km^2 pluton made up of amphibole-bearing monzogranites and rhyolitic to granitic porphyries. The pluton is asymmetrically zoned, with an altered equigranular facies to the east and a better-preserved porphyritic microgranular facies to the west. Amphibole and allanite are characteristic phases. The unit is interpreted as a hypersolvus granite with alkaline affinities, linked to rapid cooling of a surface-connected magma chamber. A Rb-Sr whole-rock age of 259 ± 2 Ma has been reported (Llambías and Sato, 1995).
- *Las Opeñas Granite* (102 km^2) is a muscovite- and cordierite-bearing granite with mesoperthitic K-feldspar megacrysts in the core of the pluton. Its elongate shape (axial ratio ~ 8.5) suggests *syn*-extensional emplacement. The pluton shows equigranular (4–7 mm) textures at the margins, whereas the central zone is characterized by the presence of K-feldspar megacrysts (up to 70 × 30 mm). Reported ages range between 258 and 254 Ma (Rb-Sr isochron dating; Llambías and Sato, 1995).
- *Agua Blanca Granite*, comprising the Agua Blanca, Bauchazeta, and Chita plutons, is exposed discontinuously. These medium-grained, weakly peraluminous granites are typically leucocratic, with scarce and late biotite indicating crystallisation under low water activity. Greisenized cupolas host molybdenum mineralization with fluorite and wolframite veins. The main phases include plagioclase, mesoperthitic K-feldspar, and quartz with subsolidus recrystallisation textures. The Chita pluton yielded a LA-MC-ICP-MS U-Pb zircon age of 260 ± 5 Ma (Sato et al., 2015), whereas a significantly older Rb-Sr whole-rock–biotite isochron age of 427 ± 15 Ma was previously reported (Sato and Kawashita, 1988).

Initially, the Tabaquito batholith—a term first introduced by Moreno et al. (2020)—was considered part of the Colangüil batholith by Llambías and Sato (1990, 1995). However, recent studies have refuted this association based on its Carboniferous age (Sato et al., 2015; Dahlquist et al., 2018; Moreno et al., 2020; Santos da Cruz et al., 2024).

Previous studies (Llambías and Sato, 1990, 1995; Sato et al., 2015) suggest that the plutonic units of the Colangüil batholith are contemporaneous with the volcanic sequences of the Choiyoi Group (andesites and rhyolites). Both were generated by the same magmatic events, which evolved from intermediate to highly silicic compositions, reflecting a continuous and dynamic magmatic evolution in the region (Rocher et al., 2024).

Subvertical dike swarms, predominantly silicic (∼90%) with minor mafic dikes (∼10%) crosscut several plutons of the batholith, particularly around the El Fierro, Los Puentes, and Conconta plutons (Llambías and Sato, 1995).

In the Tabaquito area, Carboniferous radial dike swarms (Dahlquist et al., 2024b), mostly andesitic and trending *E*-W, are crosscut by younger N-S rhyolitic dikes likely related to Permian magmatism of the Choiyoi Group (Llambías and Sato, 1995; Moreno et al., 2020).

2.2. Previous studies of the El Fierro pluton

The Permian El Fierro pluton (Fig. 2), covering ∼413 km^2 (Llambías and Sato, 1990), represents the second-largest plutonic exposure of late-stage Choiyoi plutons within the Colangüil batholith. Located in the Frontal Cordillera of Argentina (San Juan province), it intrudes the southern sector of the Carboniferous Tabaquito batholith (emplaced at 325 ± 2 Ma; Santos da Cruz et al., 2024).

Llambías and Sato (1995) described the El Fierro pluton as a massive, medium-grained (4–5 mm), equigranular gray granite with plagioclase, microperthitic K-feldspar, quartz, and biotite, with accessory zircon, apatite, ilmenite, magnetite, allanite and fluorite. Internally, fine-grained leucocratic facies (0.8–1 mm) shows transitional contacts with the coarser-grained granite and contains abundant miarolitic cavities filled with albite, quartz, muscovite, fluorite, and tourmaline, along with aplitic segregations that may include pegmatitic cores.

Moreno et al. (2020) identified small outcrops of a fine-grained leucogranite (mainly composed of quartz, alkali feldspar, plagioclase, and biotite) within the southern sector of the Tabaquito granodiorite, which may be interpreted as satellites or inliers potentially linked to the El Fierro pluton; and a coarse-grained porphyritic granite with alkali feldspar, quartz, plagioclase, biotite, and muscovite, cut by aplitic dikes. Their spatial and petrographic features support correlation with the El Fierro pluton.

Biotite and whole-rock Rb-Sr isochrons yielded an age of 257 ± 1 Ma (Llambías and Sato, 1995). A younger U-Pb zircon age of 253 ± 2 Ma for the Conconta pluton (Sato et al., 2015), another late-stage granite of the Colangüil batholith, tentatively suggests the Rb-Sr ages may represent crystallisation ages of the El Fierro pluton.

A detailed field and petrographic description based on new observations made in this study, is provided in Section 4.

3. Samples and methods

For this study, eleven representative samples were collected from the El Fierro pluton (Fig. 2), including medium- to coarse-grained porphyritic granites (TAB-21, TAB-76, TAB-80, TAB-81, TAB-83, TAB-84, TAB-85, TAB-86, TAB-87, and TAB-88) and fine- to medium-grained equigranular granites (TAB-29). For ease of reference, these facies are hereafter abbreviated as follows: CM-PG (medium- to coarse-grained porphyritic granite) and FM-EG (fine- to medium-grained equigranular granites). The sample locations are indicated on the new geological map produced in this study (Fig. 2), and their petrographic and geochemical characteristics are discussed in Section 4.

Mineral compositions were analysed for two samples (TAB-21 and TAB-29). The whole-rock major and trace element concentrations were obtained for the entire set of samples, while a subset of three samples (TAB-21, TAB-29 and TAB-76) was selected for Nd and Sr isotope analysis. One representative CM-PG sample (TAB-21) was selected for U-Pb zircon geochronology and Lu—Hf isotopic analysis. Data are presented in Tables 1–5 and Supplementary Material S1; detailed analytical procedures are provided in the Supplementary Material S2.

4. Field relations and petrography of the El Fierro pluton

4.1. Field features

The El Fierro pluton (Fig. 3) is relatively homogeneous in composition (syenogranite to monzogranite) but shows internal textural variability. Two main granite facies are recognized: (1) a medium- to coarse-grained porphyritic granite (CM-PG; Fig. 3) and (2) fine- to medium-grained equigranular cupola granites (FM-EG; Fig. 3B).

The dominant porphyritic facies (CM-PG) contains abundant phenocrysts of alkali feldspar and quartz (ca. 2–7 mm), subordinate plagioclase, and minor amounts of biotite, set in a medium- to coarse-grained groundmass mainly composed of quartz, alkali feldspar, plagioclase, biotite, and, in some cases, muscovite (locally absent). The CM-PG exhibits a steep (>55°) magmatic foliation trending NE–SW, with local N—S deviations. In certain sectors, the porphyritic character weakens, grading into coarse equigranular textures with scarce or rare phenocrysts. Locally, domains with a fine-grained matrix exceeding phenocrysts give the rock a grayish tone. This local fine-grained facies shows sharp but irregular contacts with the coarse-grained porphyritic granite, evidence of crystal transfer between both facies, as well as enclaves of the fine-grained material within porphyritic domains (Fig. 3C). These relationships suggest interactions under high-temperature conditions, with the fine-grained granite possibly still in a crystal-suspension state at the time of intrusion or reactivation of the parental magma of the coarse-grained variety. Mineralogical and geochemical similarities between the two facies (see Section 4.2) may suggest a connection within a common solidification front, although further studies are required to evaluate this interpretation.

The most evident and prominent contact of the El Fierro pluton corresponds to its intrusion into the Carboniferous Tabaquito granite, and is exposed along the eastern margin of the pluton (Fig. 2). Although partly covered by modern sediments, field relations indicate an abrupt transition from the El Fierro pluton to the Tabaquito batholith (Fig. 3A), suggesting steeply dipping contacts between the two bodies. This abrupt transition is also supported by airborne gamma-ray spectrometry image Th (Supplementary Material S3). Along the contact, the El Fierro pluton appears more pinkish due to border alteration, with interdigitated aplitic bodies at the contact. Likewise, at the satellite-image scale (Fig. 2), the contact appears irregular but locally straight, suggesting brittle intrusive mechanisms.

Mafic enclaves and xenoliths are commonly observed in the porphyritic facies (CM-PG). Enclaves (Fig. 3E, F) are rounded to ellipsoidal (size: ∼2 to 10 cm), composed of fine-grained hornblende, biotite, plagioclase, opaque minerals, quartz and alkali feldspar. The presence of quartz and feldspar phenocrysts (Fig. 3E), probably entrained from the hosting granite by mechanical transference, suggests contemporaneity and similar physical state.

Xenoliths, though less abundant, are notable within the CM-PG facies. They are centimetric (up to ∼6 cm; Fig. 3G), with angular shapes, and composed of metamorphic rocks (e.g., pelites, psammites, and metaquartzites).

The FM-EG facies is light gray to whitish, fine-grained and equigranular, with alkali feldspar, quartz, plagioclase, biotite, and subordinate muscovite. Miarolitic cavities filled with quartz and feldspar are locally present (Fig. 3D), supporting its interpretation as a cupola facies.

This facies displays a restricted distribution, forming subcircular to elongated bodies in map view, recognized in the northeastern and central sectors of the El Fierro pluton, aligned predominantly along a north–south trend. Several of these bodies form positive reliefs or dome-shaped outcrops, reflecting their greater resistance to erosion. According to Llambías and Sato (1995), this facies occurs within the inner part of the pluton, although it can also appear as small-size satellites or inliers within the Tabaquito granodiorite, close to the contact with the El Fierro pluton (Moreno et al., 2020).

In vertical section, the FM-EG occupies concordant external

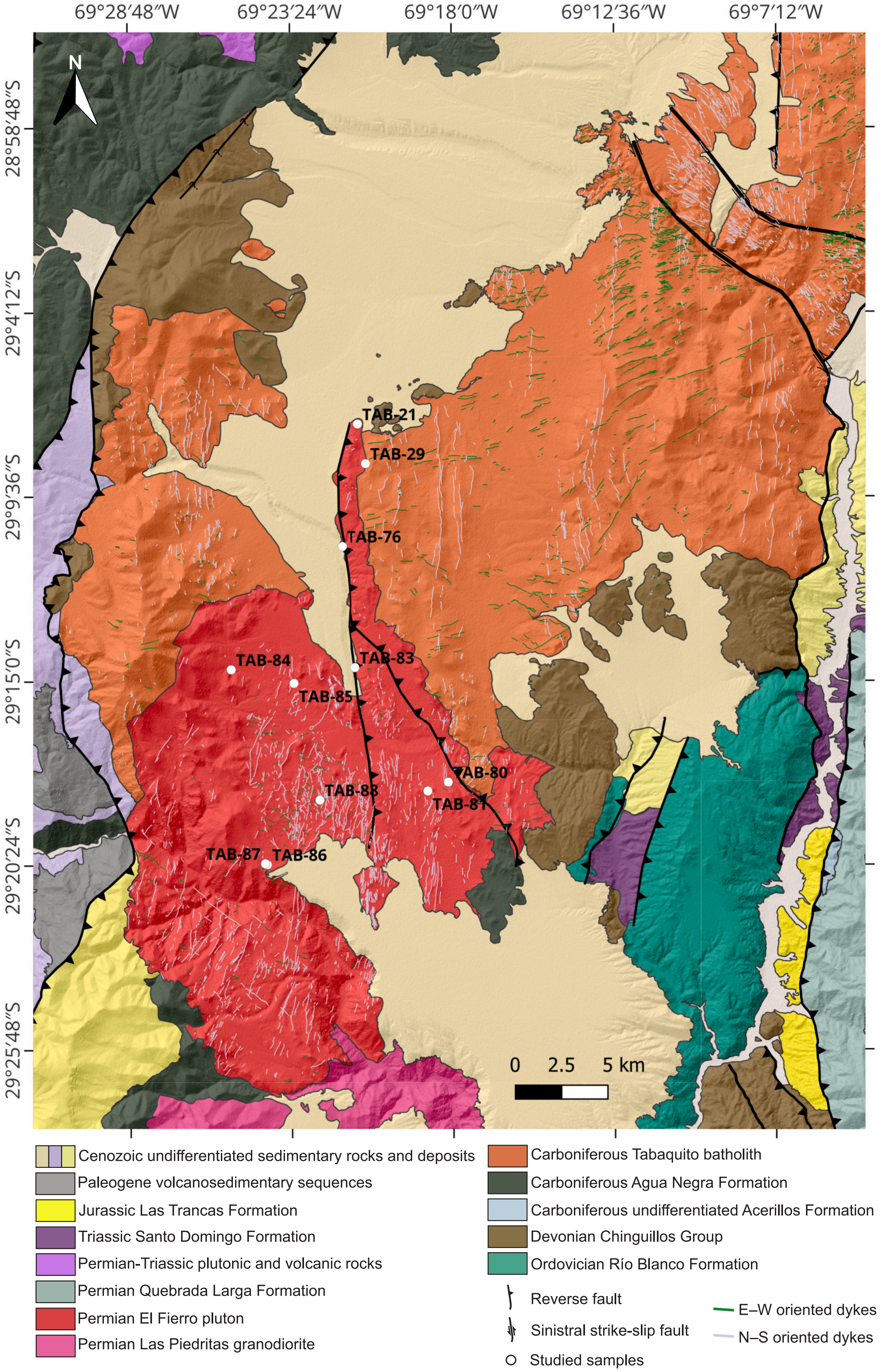

Fig. 2. Detailed geological map of the El Fierro Pluton and surrounding units, showing the location of the collected samples. Green lines represent E–W dikes and gray lines indicate N—S dikes. (For interpretation of the references to colour in this figure legend, the reader is referred to the web version of this article.)

Table 1
EMP analyses of feldspars from the El Fierro pluton.

Sample	TAB-21	TAB-21	TAB-21	TAB-21	TAB-21	TAB-21	TAB-21	TAB-21	TAB-21	TAB-21	TAB-21	TAB-21
Phase[1]	Plg	Plg	Plg	Plg	Plg	Plg	Plg	Plg	Plg	Plg	Kfs	Kfs
Analysis	1	2	3	4	5	6	7	8	9	10	1	2
SiO_2	64.14	66.47	61.93	61.71	62.72	64.97	64.60	64.17	65.62	64.53	63.24	63.76
Al_2O_3	22.33	20.30	23.10	23.03	22.85	21.55	22.13	22.09	21.28	21.53	19.14	19.40
FeO	0.06	0.05	0.06	0.02	0.09	0.06	0.05	0.03	0.00	0.00	0.18	0.08
SrO	0.00	0.00	0.00	0.00	0.00	0.00	0.00	0.00	0.00	0.00	0.00	0.00
BaO	0.00	0.00	0.02	0.11	0.16	0.00	0.00	0.05	0.00	0.07	0.00	0.00
CaO	2.40	0.40	3.68	3.78	3.31	1.48	2.01	2.10	1.20	1.88	0.03	0.02
Na_2O	10.00	11.07	8.70	8.47	9.18	10.28	10.28	10.11	10.76	10.08	1.58	2.02
P_2O_5	0.00	0.04	0.02	0.00	0.03	0.04	0.02	0.02	0.03	0.05	0.00	0.03
K_2O	0.55	0.25	0.89	1.12	0.75	0.38	0.39	0.43	0.40	0.55	14.64	13.95
Total	99.48	98.57	98.41	98.24	99.09	98.76	99.48	98.99	99.29	98.69	98.81	99.25
Ab%	85.5	96.6	76.8	75.0	79.8	90.6	88.3	87.5	92.1	87.8	14.1	18.0
Or%	3.1	1.4	5.2	6.5	4.3	2.2	2.2	2.5	2.2	3.2	85.8	81.9
An%	11.3	1.9	18.0	18.5	15.9	7.2	9.5	10.0	5.7	9.0	0.2	0.1

Sample	TAB-29	TAB-29	TAB-29	TAB-29	TAB-29	TAB-29	TAB-29	TAB-29	TAB-29	TAB-29
Phase[1]	Plg	Plg	Plg	Plg	Plg	Plg	Kfs	Kfs	Kfs	Kfs
Analysis	1	2	3	4	5	6	1	2	3	4
SiO_2	65.03	64.54	66.23	64.67	65.49	67.33	64.05	64.57	64.24	63.63
Al_2O_3	21.28	21.96	22.01	21.89	21.50	20.31	19.29	19.51	19.35	18.97
FeO	0.02	0.09	0.04	0.01	0.00	0.01	0.00	0.03	0.00	0.06
SrO	0.00	0.00	0.00	0.00	0.00	0.00	0.00	0.00	0.00	0.00
BaO	0.02	0.00	0.05	0.00	0.14	0.16	0.09	0.09	0.00	0.00
CaO	1.59	2.06	1.85	2.03	1.47	0.10	0.09	0.08	0.08	0.04
Na_2O	10.35	9.84	10.07	9.92	10.53	11.29	2.98	3.22	3.62	1.93
P_2O_5	0.01	0.05	0.00	0.04	0.01	0.01	0.02	0.01	0.02	0.03
K_2O	0.38	0.43	0.46	0.63	0.50	0.34	12.77	12.22	11.58	13.90
Total	98.68	98.98	100.71	99.18	99.64	99.55	99.29	99.73	98.89	98.56
Ab%	90.2	87.4	88.4	86.6	90.2	97.6	26.1	28.5	32.1	17.4
Or%	2.2	2.5	2.7	3.6	2.8	1.9	73.5	71.1	67.5	82.4
An%	7.7	10.1	9.0	9.8	7.0	0.5	0.4	0.4	0.4	0.2

1: Kfs, alkali feldspar; Plg, plagioclase.

positions, grading upward from the porphyritic granite to the fine-grained equigranular granite. Within this transitional zone, crystal transfer is evident, since phenocrysts abundance gradually decreases toward the equigranular facies across a band of approximately one meter.

The pluton is intruded exclusively by predominantly andesitic north–south trending dikes, likely Permian (Fig. 2). Notably, east–west subvolcanic dikes of proven Carboniferous age, which are abundant in the Tabaquito batholith (Dahlquist et al., 2024b), are absent.

4.2. *Petrography and modal composition*

The El Fierro pluton is hololeucocratic (M $<$ 10%), consisting of syeno-monzogranites with a dominant coarse- to medium-grained porphyritic texture (CM-PG) and subordinate fine- to medium-grained equigranular facies (FM-EG).

The CM-PG (Fig. 4) facies is characterized by phenocrysts (~15–80 vol%) of alkali feldspar, quartz, plagioclase, and biotite, set in a quartz-feldspathic matrix (~15–20 vol%) with biotite. Matrix minerals are generally <1 mm, whereas phenocrysts display variable dimensions, reaching up to 12 × 6 mm in alkali feldspar. The main mineral assemblage consists of quartz (21–44%), mesoperthitic alkali feldspar (29–49%), and plagioclase (17–30%), with biotite (2–7%) as a varietal mineral. The main accessory minerals are apatite, zircon, epidote, and muscovite, along with minor opaque phases and allanite. Both primary epidote and allanite (Fig. 4A, B) are commonly associated with biotite. Secondary minerals include muscovite-sericite, chlorite, and epidote. Locally, these rocks display graphic and/or granophyric textures and occasionally contain biotite clots (Fig. 4B) with inclusions of opaque minerals, apatite, allanite, and zircon.

The FM-EG (Fig. 4D) facies shows an aplitic equigranular texture, with domains showing well-developed graphic intergrowths (Qtz + Kfs). Alkali feldspar (~36%) is predominantly anhedral, locally perthitic, with widespread alteration to clay. Plagioclase (~25%) shows polysynthetic twinning and sericitization. Quartz (~34%) exhibits irregular embayed/indented margins and sutured contacts with adjacent minerals. Biotite occurs bordering quartz and feldspars, filling fractures, and contains zircon inclusions. Muscovite is scarce, occurring in interstitial positions or replacing plagioclase. Epidote occurs as a secondary phase. Accessory minerals are zircon, apatite, and muscovite, with rare opaque oxides, occurring as small reddish crystals included in biotite, quartz, and alkali feldspar, or occupying interstitial sites.

5. Mineral chemistry

5.1. *Feldspars*

Plagioclase in the CM-PG facies has oligoclase cores ($An_{11–18}$) with albite rims ($An_{2–10}$) (Supplementary Material S4; Table 1). The composition of alkali feldspar ranges from Or_{82} to Or_{86} (Supplementary Material S4 and Table 1).

Plagioclase in the FM-EG facies is more sodic showing albite compositions ($An_{1–10}$; Supplementary Material S4), with the alkali feldspar being also less potassic with compositions varying between Or_{68} and

Table 2
EMP analyses of micas from the El Fierro pluton.

Sample	TAB-21	TAB-21	TAB-21	TAB-21	TAB-21	TAB-21	TAB-29	TAB-29	TAB-29	TAB-29	TAB-29	TAB-29
Phase[1]	Bt	Bt	Bt	Bt	Bt	Bt	Bt	Bt	Bt	Bt	Bt	Bt
Analysis	1	2	3	4	5	6	1	2	3	4	5	6
SiO_2	35.88	35.24	33.06	33.69	34.81	35.14	36.52	35.07	36.05	37.43	38.17	37.64
TiO_2	1.23	0.92	2.21	2.53	1.93	1.56	0.90	1.09	0.30	0.35	0.13	0.36
Al_2O_3	22.00	21.06	19.66	19.33	19.60	21.01	21.93	21.90	21.66	22.73	23.41	22.89
FeO	22.52	24.04	25.66	25.28	23.75	25.39	22.08	23.13	22.26	21.22	21.18	20.63
MnO	0.31	0.51	0.46	0.39	0.43	0.45	0.61	0.76	0.88	0.85	0.88	0.62
MgO	1.63	1.70	1.65	1.62	1.62	1.69	0.39	0.31	0.34	0.34	0.36	0.36
CaO	0.00	0.00	0.01	0.00	0.01	0.02	0.00	0.00	0.00	0.01	0.02	0.03
Na_2O	0.26	0.18	0.24	0.21	0.28	0.16	0.35	0.28	0.26	0.27	0.32	0.29
Cr_2O_3												
ZnO	0.04	0.06	0.05	0.10	0.00	0.00	0.11	0.09	0.10	0.00	0.12	0.12
K_2O	9.43	9.38	9.20	9.36	9.40	9.61	9.29	9.08	9.25	9.40	9.14	9.39
BaO	0.00	0.23	0.07	0.00	0.42	0.05	0.00	0.25	0.00	0.02	0.00	0.00
Li_2O*	0.55	0.36			0.24	0.33	0.73	0.31	0.60	1.00	1.21	1.06
F	2.48	2.72	2.93	2.60	2.78	1.72	4.20	2.66	3.49	3.76	3.73	4.47
Cl	0.09	0.12	0.18	0.26	0.30	0.19	0.13	0.15	0.11	0.12	0.09	0.07
Total	96.43	96.53	95.39	95.37	95.55	97.32	97.23	95.09	95.30	97.50	98.76	97.93
–O = F + Cl	1.06	1.17	1.28	1.15	1.24	0.77	1.80	1.15	1.49	1.61	1.59	1.90
Total	95.36	95.36	94.11	94.22	94.31	96.55	95.44	93.94	93.80	95.89	97.17	96.03
Formula based on 22 oxygens												
Si	5.581	5.570	5.400	5.471	5.602	5.487	5.717	5.599	5.742	5.766	5.768	5.786
Ti	0.144	0.109	0.271	0.309	0.234	0.183	0.106	0.131	0.036	0.040	0.014	0.041
Al	4.033	3.923	3.785	3.699	3.717	3.866	4.046	4.120	4.066	4.126	4.169	4.147
Fe	2.929	3.177	3.505	3.432	3.196	3.315	2.890	3.088	2.965	2.733	2.676	2.652
Mn	0.041	0.069	0.064	0.054	0.058	0.060	0.081	0.102	0.119	0.112	0.113	0.081
Mg	0.379	0.401	0.401	0.392	0.388	0.393	0.091	0.075	0.081	0.077	0.081	0.083
Ca	0.000	0.000	0.002	0.000	0.001	0.003	0.000	0.000	0.000	0.001	0.002	0.005
Na	0.080	0.057	0.077	0.065	0.086	0.049	0.105	0.088	0.081	0.082	0.094	0.085
Cr	0.000	0.000	0.000	0.000	0.000	0.000	0.000	0.000	0.000	0.000	0.000	0.000
Zn	0.005	0.008	0.006	0.012	0.000	0.000	0.012	0.011	0.011	0.000	0.014	0.014
K	1.871	1.891	1.917	1.939	1.930	1.914	1.855	1.849	1.879	1.847	1.762	1.841
Ba	0.000	0.014	0.004	0.000	0.026	0.003	0.000	0.016	0.000	0.001	0.000	0.000
F	1.220	1.359	1.513	1.335	1.415	0.849	2.079	1.343	1.758	1.832	1.782	2.173
Cl	0.023	0.032	0.051	0.072	0.081	0.050	0.034	0.040	0.030	0.030	0.024	0.019
Li	0.342	0.230	0.000	0.000	0.153	0.209	0.461	0.200	0.382	0.618	0.736	0.654
XMg	0.114	0.112	0.103	0.102	0.108	0.106	0.030	0.024	0.027	0.027	0.029	0.030

TAB-21	TAB-21	TAB-21	TAB-21	TAB-21	TAB-21	TAB-21	TAB-21	TAB-21
Ms	Ms	Ms	Ms	Ms	Ms	Ms	Ms	Ms
1	2	3	4	5	6	7	8	9
44.35	45.10	43.93	43.77	43.48	43.20	43.08	43.40	43.61
0.46	0.51	0.83	1.12	0.75	0.55	0.84	0.50	0.32
29.71	29.79	29.93	31.30	28.97	28.91	28.76	31.73	30.77
6.93	6.66	6.11	5.20	6.97	6.69	6.66	5.97	6.43
0.15	0.06	0.15	0.15	0.15	0.13	0.10	0.06	0.11
1.14	1.10	0.98	0.84	1.10	1.05	1.10	0.31	0.41
0.00	0.00	0.01	0.00	0.00	0.01	0.02	0.00	0.00
0.47	0.38	0.49	0.60	0.55	0.40	0.39	0.45	0.47
0.00	0.00	0.00	0.00	0.01	0.04	0.03	0.08	0.02
10.28	10.59	10.32	10.24	10.13	10.34	10.18	10.45	10.76
0.00	0.07	0.05	0.00	0.19	0.02	0.00	0.00	0.00
1.51	1.51	1.83	1.43	1.86	1.43	1.70	1.25	2.06
2.76	2.76	3.19	2.65	3.22	2.65	3.02	2.39	3.48
0.03	0.00	0.01	0.00	0.01	0.00	0.01	0.01	0.01
97.79	98.55	97.84	97.29	97.38	95.42	95.89	96.59	98.45
1.17	1.16	1.35	1.12	1.36	1.12	1.27	1.01	1.47
96.62	97.39	96.49	96.18	96.03	94.30	94.61	95.59	96.98
6.114	6.159	6.060	6.009	6.065	6.112	6.080	6.012	6.010
0.047	0.053	0.086	0.115	0.079	0.058	0.089	0.052	0.033
4.827	4.794	4.866	5.064	4.763	4.820	4.783	5.180	4.997
0.799	0.761	0.705	0.597	0.813	0.791	0.786	0.692	0.741
0.018	0.007	0.018	0.018	0.017	0.015	0.012	0.007	0.013
0.234	0.225	0.201	0.171	0.229	0.221	0.232	0.064	0.083
0.000	0.000	0.002	0.000	0.000	0.001	0.003	0.000	0.000

(*continued on next page*)

Table 2 (*continued*)

TAB-21	TAB-21	TAB-21	TAB-21	TAB-21	TAB-21	TAB-21	TAB-21	TAB-21
Ms	Ms	Ms	Ms	Ms	Ms	Ms	Ms	Ms
1	2	3	4	5	6	7	8	9
0.127	0.102	0.131	0.159	0.148	0.110	0.108	0.120	0.126
0.000	0.000	0.000	0.000	0.000	0.000	0.000	0.000	0.000
0.000	0.000	0.000	0.000	0.001	0.004	0.003	0.008	0.002
1.808	1.845	1.816	1.793	1.803	1.866	1.833	1.846	1.891
0.000	0.004	0.003	0.000	0.011	0.001	0.000	0.000	0.000
1.203	1.192	1.391	1.150	1.420	1.185	1.348	1.047	1.516
0.006	0.000	0.003	0.001	0.001	0.001	0.002	0.002	0.002
0.838	0.830	1.016	0.791	1.041	0.815	0.967	0.696	1.140
0.227	0.228	0.222	0.223	0.220	0.218	0.228	0.084	0.101

1: Bt, biotite; Ms., muscovite.

[*] Li contents calculated from expressions derived by Tischendorf et al. (2004) and Breiter et al. (2017).

Or_{82} (Supplementary Material S4 and Table 1).

5.2. Trioctaedral mica

Trioctahedral mica from both facies is siderophyllite (Supplementary Material S4) with very uniform and low $Mg/(Mg + Fe^{2+})$ in each facies (CM-PG: 0.10–0.11; FM-EG: 0.02–0.03) (Table 2). Li contents have been calculated according to Breiter et al. (2017) for micas containing 34–43 wt% SiO_2 and < 8 wt% MgO, since our data do not satisfy the chemical requirement of the empirical expressions derived by Tischendorf et al. (2004). The Li contents in the FM-EG are those expected in siderophyllite sensu stricto (av. 0.8 wt% Li_2O; Tischendorf et al., 2007) with an average value of 0.82 wt% Li_2O (range: 0.31–1.22 wt%), whereas siderophyllite from the CM-PG is poorer in Li (av. 0.37 wt%; range: 0.24–0.55 wt%) (Table 2). F contents are high, with values of 0.85–1.51 apfu in the CM-PG facies and 1.34–2.17 apfu in the FM-EG facies (Table 2). Cl contents are low, being slightly higher in the CM-PG facies (0.02–0.08 apfu) than in the FM-EG facies (0.02–0.04 apfu).

In the TiO_2–FeO–MgO diagram of Nachit et al. (2005), some analyses of the biotite from CM-PG plotted in the field of the primary magmatic biotites (Fig. 5A), whereas other plot as reequilibrated biotites (Fig. 5A). This suggests that biotite from the CM-PG may have undergone certain degree of reequilibration, which is also in accordance with Al^{VI} values >1.1 apfu that are typical values of reequilibrated and neoformed biotites ($Al^{VI} > 1$ apfu; Nachit et al., 2005). On the other hand, analyses of the biotite from the FM-EG mostly plot in the field of neoformed biotites (Fig. 5A), which is also supported by their higher Al^{VI} values and lower TiO_2 content than the biotites from the CM-PG (Table 2).

5.3. Dioctahedral white mica

The white mica of the CM-PG facies is classified as phengite (Supplementary Material S4) and shows primary compositions (Fig. 5B) with relatively high Na (0.10–0.16 apfu) and Ti (0.03–0.12 apfu), high F (1.05–1.52 apfu), and $Mg/(Mg + Fe^{2+})$ ratio ranging from 0.08 to 0.23 (Table 2). The Li content can be relatively high reaching up to1.14 apfu (Table 2).

5.4. Melt fluorine and chlorine contents

Whole-rock fluorine and chlorine data are not available for the El Fierro pluton. Nevertheless, the high F contents of biotite, along with their very high atomic Fe/(Fe + Mg) ratios (>0.85) (Fig. 5C), strongly suggest that the magmas had relatively high HF/H_2O ratios. Melt fluorine and chlorine contents were calculated from biotite composition using expressions derived by Muñoz (1984, 1992) (Supplementary Material S5), since the Mg/(Mg + Fe + Mn) ratio of the analysed biotites is lower than 0.2, thus precluding the use of the equations derived by London (1997). Furthermore, this method has been previously applied in Argentine metaluminous to slightly peraluminous A-type granites with consistent results (Dahlquist et al., 2010; Morales Cámera et al., 2022). These equations relate the activity of F and Cl in biotite to the ratios $\log(fH_2O/fHF)$ and $\log(fH_2O/fHCl)$, and propagate these activity ratios through the biotite–melt equilibrium expressions. As a result, the Muñoz model directly yields halogen concentrations in the melt in ppm.

The calculated F contents (Fig. 5D) are high, with the CM-PG facies showing values of 6101–13,749 ppm and the FM-EG facies displaying higher values (13153–31,442 ppm), which in principle are consistent with its more evolved character.

The calculated Cl content is lower than the F content but still relatively high, ranging between 269 and 1052 ppm in the CM-PG facies and between 322 and 557 ppm in the FM-EG facies.

6. U-Pb zircon dating

Cathodoluminescence (CL; Supplementary Material S6) images of zircon grains from sample TAB-21 (CM-PG facies) reveal morphological variability. Most grains are prismatic with well-developed pyramidal terminations, although stubby subhedral to anhedral grains are also present. Some grains are rounded or partially corroded. Grain lengths range from ~100 μm to ca. 300 μm, with aspect ratios varying from slender prisms to nearly equidimensional grains. Several zircon grains exhibit internal fractures, incomplete edges, or irregular surfaces. Concentric oscillatory zoning is commonly well developed in both cores and rims, whereas some grains show homogeneous textures or recrystallised cores surrounded by dark overgrowths. In addition, certain zircon grains present sector zoning and mineral inclusions.

Analyses were mainly performed on the magmatic growth zones of zircon to constrain its crystallisation age (Supplementary Material S6).

Thirty-seven LA-MC-ICP-MS U-Pb zircon analyses from sample TAB-21 yield a $^{238}U/^{206}Pb$ weighted mean age of 264 ± 3 Ma, although with a relatively high MSWD = 2.4 (data reported in Supplementary Material S1). Notably, the range of crystallisation ages is significantly broad, varying between 258 and 285 Ma.

Using the methodology largely described by Dahlquist et al. (2024c) and Santos da Cruz et al. (2024) we distinguish three age populations, which are shown in Fig. 6.

The youngest age population is interpreted as an age affected by Pb loss (only three analyses out of 22; one of these is from a zircon grain with two analyses that yielded distinct ages—263 and 253 Ma—suggesting that the younger age reflects partial rejuvenation caused by Pb loss in that sector), with subsequent partial resetting of the isotopic clock, while the other two populations are considered zircon antecrysts and autocrysts, respectively (Fig. 6), as discussed in Section 10.1. In addition, two individual older ages of 279 ± 6 and 285 ± 9 Ma are considered the oldest crystallisation event. An age of 402 ± 11 Ma is assumed as an inherited zircon age.

Subsequently, weighted mean ages of each zircon age populations can then be calculated yielding three ages (Fig. 7A-D): 251 ± 7 Ma (n = 3, MSWD = 0.11, age affected by partial Pb loss), 262 ± 2 Ma (n = 12,

Table 3
Whole-rock compositions from the El Fierro granites.

Sample:	TAB-21	TAB-29	TAB-76	TAB-81	TAB-86	TAB-88	TAB-80	TAB-83	TAB-84	TAB-85	TAB-87
Rock Type[a]:	CM-PG	FM-EG	CM-PG	CM-PG	CM-PG	CM-PG	CM-PG	CM-PG	CM-PG	CM-PG	CM-PG
Major elements (wt%)											
SiO_2	75.55	75.17	76.72	74.70	71.90	75.38	76.53	72.66	70.82	72.14	71.12
TiO_2	0.11	0.02	0.13	0.39	0.42	0.34	0.11	0.18	0.27	0.38	0.48
Al_2O_3	12.68	13.23	12.07	11.16	13.64	11.86	12.87	13.88	13.75	13.87	13.97
FeO	1.30	0.93	1.19	2.89	2.57	2.48	1.26	1.78	2.34	3.15	3.22
MnO	0.02	0.03	0.02	0.00	0.04	0.00	0.04	0.03	0.04	0.05	0.05
MgO	0.11	0.01	0.18	0.45	0.65	0.42	0.19	0.31	0.36	0.47	0.65
CaO	0.44	0.36	0.49	1.22	1.37	1.20	0.50	0.35	1.02	1.27	1.55
Na_2O	2.86	3.53	3.13	3.01	3.03	3.02	3.75	3.36	3.41	3.45	2.98
K_2O	5.20	4.64	5.18	4.88	5.37	4.73	4.58	5.67	5.03	4.53	4.82
P_2O_5	0.03	0.01	0.05	0.15	0.18	0.11	0.04	0.06	0.09	0.13	0.18
LOI	1.20	1.40	0.65	0.73	0.75	0.39	0.53	0.67	0.74	1.01	0.66
Total	99.50	99.33	99.82	99.58	99.91	99.92	100.41	98.94	97.87	100.44	99.68
XFe	0.92	0.99	0.87	0.87	0.80	0.86	0.87	0.85	0.87	0.87	0.83
MALI	7.62	7.81	7.82	6.67	7.03	6.54	7.83	8.68	7.42	6.71	6.26
ASI	1.14	1.15	1.04	0.90	1.03	0.97	1.07	1.13	1.06	1.08	1.08
Trace elements (ppm)											
Li			86.7	76.2	96.7	64.6	296	84	156	182	141
Be	3.00	11.0	4.19	3.30	3.40	3.10	31.1	5.09	4.44	5.29	6.79
Sc	14.0	16.0	5.16	9.80	8.00	8.70	14.0	18.5	19.5	24.9	18.1
V			8.30	19.6	28.1	12.9	5.58	8.87	15.06	24.0	38.0
Cr				2.70	7.60	2.20	1.77	1.68	2.37	3.14	6.65
Co			28.9	11.4	26.8	8.20	4.47	18.1	12.9	8.30	34.9
Ni			0.69	1.10	3.50	0.70	1.08	1.12	1.21	1.57	3.21
Cu			0.45	3.10	2.60	0.80	1.29	1.79	0.77	1.43	4.37
Zn			23.3	71.5	57.2	57.1	53.6	73.1	76.8	127	94.0
Cs	15.0	27.9	5.09	9.50	9.80	6.40	41.1	12.9	11.2	10.8	15.1
Rb	348	540	287	205	226	171	557	400	338	334	344
Sr	31.8	11.5	19.4	49.7	80.2	43.2	22.9	44.7	41.3	56.0	78.1
Ba	100	8.00	176	220	328	191	59.4	154	161	214	262
La	37.1	9.30	21.4	39.7	38.0	25.7	35.2	46.6	65.4	90.5	83.1
Ce	98.0	29.2	40.3	98.6	88.6	62.4	91.2	116	154	210	184
Pr	11.06	3.89	6.22	11.7	10.3	7.70	11.3	14.1	18.2	24.7	21.8
Nd	38.5	14	24	44.4	37.9	30.2	42.6	53.2	68.8	93.4	81.0
Sm	10.05	5.90	5.57	10.0	7.90	7.00	11.7	12.6	15.3	20.6	17.1
Eu	0.17		0.27	0.40	0.60	0.30	0.22	0.5	0.46	0.56	0.75
Gd	9.12	7.69	4.83	9.70	7.40	6.60	9.25	9.62	11.1	15.5	12.7
Tb	1.64	1.55	0.78	1.20	0.80	0.80	1.57	1.49	1.52	2.22	1.80
Dy	9.55	9.67	4.59	6.5	4.4	4.5	8.85	7.53	7.93	12.0	9.78
Ho	2.00	2.09	0.91	1.10	0.70	0.70	1.68	1.49	1.39	2.15	1.78
Er	5.64	6.43	2.63	3.10	2.00	2.20	4.95	3.93	3.78	5.94	4.97
Tm	0.82	1.05	0.40	0.30	0.20	0.20	0.79	0.68	0.53	0.83	0.69
Yb	5.16	7.28	2.65	2.50	1.70	1.90	5.01	3.64	3.27	5.17	4.25
Lu	0.78	1.12	0.37	0.30	0.10	0.20	0.77	0.66	0.48	0.75	0.61
U	4.50	9.40	2.07	2.50	2.60	3.20	7.58	5.53	4.93	6.28	4.83
Th	22.0	12.0	9.7	22.0	18.8	18.6	22.2	25.4	32.2	46.7	39.8
Yb	52.5	57.1	26.1	27.9	18.5	20.0	45.4	35.4	35.7	57.4	48.9
Nb	17.9	21.5	13.4	17.6	14.5	12.7	26.3	27.2	27.8	35.7	27.1
Zr	75.4	41.0	161	78.3	81.4	75.1	118	172	212	281	276
Hf	4.10	3.90	4.75	2.40	2.20	2.30	4.40	4.73	4.50	5.78	4.69
Ta	2.10	4.30	0.90	3.60	3.50	3.90	3.39	2.79	2.00	2.80	2.40
Ga	20.4	23.7	23.2	25.1	23.3	18.2	31.7	35	38.6	44.4	39.4
Pb	23.8	27.4	18.4	19.6	27.2	16.3	31.6	29.8	30.8	31.6	30.8
$(La/Lu)_N$	4.94	0.862	6.00	13.7	39.4	13.3	4.74	7.32	14.2	12.5	14.1
Eu/Eu*	0.054		0.159	0.124	0.239	0.135	0.064	0.138	0.108	0.096	0.155
10000*Ga/Al	3.04	3.38	3.63	4.25	3.23	2.90	4.65	4.77	5.30	6.05	5.33
Zr + Nb + Y + Ce	244	149	241	222	203	170	281	350	430	584	536
$(Ce/Pb)_N$	0.369	0.095	0.196	0.451	0.292	0.343	0.258	0.348	0.448	0.593	0.534
$(Th/Nb)_N$	10.2	4.62	5.99	10.3	10.7	12.1	6.991	7.726	9.593	10.8	12.1
$(La/Nb)_N$	2.10	0.44	1.62	2.29	2.66	2.05	1.36	1.74	2.39	2.58	3.11
$(Y/Nb)_N$	0.449	0.406	0.298	0.243	0.195	0.241	0.264	0.199	0.197	0.246	0.276
T_{Zr}	737	691	792	717	729	721	767	801	813	840	838
T_{Ap}	758	665	884	993	965	968	844	788	855	896	921

[a] : CM-PG, medium- to coarse-grained porphyritic granite; FM-EG, fine- to medium-grained equigranular granites.

Table 4
Nd and Sr compositions of the El Fierro granites.

Sample	Facies[1]	Nd isotopic composition								
		Age (Ma)	Sm ppm	Nd ppm	$^{147}Sm/^{144}Nd$	$^{143}Nd/^{144}Nd$	Error ($\pm 2\sigma$)	$^{143}Nd/^{144}Nd_t$	εNd_i	T_{DM} (Ma)
TAB-21	CM-PG	262	10.05	38.05	0.158	0.5124	$1*10^{-6}$	0.51213	−3.31	1307
TAB-29	FM-EG	262	5.9	14	0.255	0.51258	$1*10^{-6}$	0.51214	−3.16	1294
TAB-76	CM-PG	262	5.57	24	0.14	0.51237	$1*10^{-6}$	0.51213	−3.3	1306

1: CM-PG – medium- to coarse-grained porphyritic granite; FM-EG - fine- to medium-grained equigranular granite.
Epsilon-Sr (εSr) values were calculated relative to the present-day uniform reservoir (UR):
$(^{86}Rb/^{87}Sr)_{today} = 0.0816$; $(^{87}Sr/^{86}Sr)_{today} = 0.7045$.
Epsilon-Nd (εNd) values were calculated relative to the present-day chondritic uniform reservoir (CHUR):
$(^{143}Nd/^{144}Nd)_{today} = 0.512638$; $(^{143}Sm/^{144}Nd)_{today} = 0.1967$.

Sr isotopic compositions							
Age (Ma)	Rb ppm	Sr ppm	$^{87}Rb/^{86}Sr$	$^{87}Sr/^{86}Sr$	Error ($\pm 2\sigma$)	$^{87}Sr/^{86}Sr_t$	εSr_i
262	348.4	31.8	32.11	0.83602	$3*10^{-6}$	0.71633	172
262	540	11.5	143.932	1.30709	$3*10^{-6}$	0.77061	943
262	287	19.4	43.079	0.76994	$3*10^{-6}$	0.60937	−1347

Table 5
Laser ablation Hf isotope data for igneous dated zircon from sample TAB-21.

Grain spot	$^{176}Hf/^{177}Hf$	± 2 σ	$^{176}Lu/^{177}Hf$	± 2 σ	Age (Ma)	ƐHf (t)	T^{C}_{DM} (Ga)	T^{B}_{DM} (Ga)
1.1	0.28265	0.00007	0.000391	0.000006	274	1.25	1.15	1.96
3.1	0.28251	0.00007	0.000922	0.000006	253	−4.26	1.48	2.60
4.1	0.28254	0.00006	0.00097	0.00004	265	−2.94	1.41	2.45
5.1	0.28251	0.00007	0.0013	0.0002	264	−4.08	1.48	2.58
6.1	0.28253	0.00007	0.00083	0.00002	240	−3.82	1.44	2.54
12.1	0.28257	0.00006	0.00111	0.00009	258	−2.06	1.34	2.34
16.1	0.28259	0.00007	0.000849	0.000006	259	−1.28	1.30	2.25
17.1*	0.28261	0.00008	0.00049	0.00002	402	2.63	1.16	1.86
18.1	0.28265	0.00006	0.00103	0.00008	267	0.98	1.16	1.98
19.1	0.2826	0.00007	0.00061	0.00001	262	−0.82	1.27	2.20
20.1	0.28266	0.00007	0.00071	0.00003	258	1.20	1.14	1.95
22.1	0.2825	0.00007	0.00083	0.00006	285	−3.90	1.48	2.57
25.1	0.2825	0.00007	0.000417	0.000009	263	−4.30	1.49	2.61
26.1	0.28242	0.00007	0.0011	0.0003	275	−7.00	1.67	2.93

t = crystallisation ages are from the sample TAB-21 (*Supplementary Data File S1*). T = model age.
$^{176}Hf/^{177}Hf_{CHUR(t)}$ is calculated using the t value for each analysis.
A two–stage continental model (T^{C}_{DM}) was calculated using the initial $^{176}Hf/^{177}Hf$ of zircon and the $^{176}Lu/^{177}Hf = 0.015$ ratio for the lower continental crust (Griffin et al., 2004), and $^{176}Lu/^{177}Hf = 0.038697$ and $^{176}Hf/^{177}Hf = 0.283237$ DM values from Vervoort and Kemp (2016). Decay constant for ^{176}Lu of 1.867×10^{-11} was used (Söderlund et al., 2004). The present–day chondritic (CHUR) ratios of $^{176}Hf/^{177}Hf = 0.282785$ and $^{176}Lu/^{177}Hf = 0.0336$ from Bouvier et al. (2008) were adopted to calculate εHf values.
εHf_t and T^{C}_{DM} parameters are calculated using the formulas reported by Yang et al. (2007).
T^{B}_{DM} calculation following Bea et al. (2018).
* Inherited zircon.

MSWD = 0.40, zircon autocysts), and 273 ± 5 Ma (*n* = 5, MSWD = 0.19, zircon antecrysts). The age populations are shown in equivalent Concordia diagram (Fig. 8).

7. Hf zircon isotope data

εHf_t (t = crystallisation Permian age reported in Supplementary Material S1) values for the sample TAB-21 (*n* = 14) show a wide range from −7.0 to +1.25 (*n* = 13), although negative values are largely dominant (*n* = 10) (Table 5). The two-stage Hf model ages (T_{DM}) calculated according to Griffin et al. (2002) range from 1.15 to 1.66 Ga (Table 5). However, when we consider the recommendations by Bea et al. (2018) the obtained model ages are clearly older, varying between 1.95 and 2.93 Ga (Table 5).

8. Whole-rock chemistry

In this section we use eleven samples from the El Fierro pluton (one sample of the FM-EG and ten of the main CM-PG) in comparison with samples from the El Fierro pluton and Los Puentes pluton from Llambías and Sato (1995) to characterise geochemically the magmatism of the El Fierro pluton.

All the studied samples are clearly ferroan ($FeO_T/(MgO + FeO_T)$ by weight = 0.80–0.92) with the FM-EG showing the highest ($FeO_T/(MgO + FeO_T)$) value of 0.99 (Fig. Fig. 9A; Table 3). They are alkali-calcic to calc-alkalic (MALI = 6.26–8.68) and metaluminous to weakly peraluminous (ASI = 0.89–1.15) (Fig. 9; Table 3), with most samples being peraluminous, as indicated by the presence of primary muscovite. Consequently, most samples plot as low peraluminous granites (Fig. 9D) in the A–B diagram of Debon and Le Fort (1983) modified by Villaseca et al. (1998), although various samples plot as highly felsic peraluminous granites (Fig. 9D). All of this is consistent with the data reported by Llambías and Sato (1995) for the late-stage Choiyoi granites (Fig. 9), indicating a weakly peraluminous A-type composition that is also consistent with the trace-element data described below. Conversely, the compositions of the El Fierro pluton and the rest of the late-stage Choiyoi granites strongly contrast with the obvious metaluminous, magnesian and calc-alkalic compositions of the granitoids of the early-

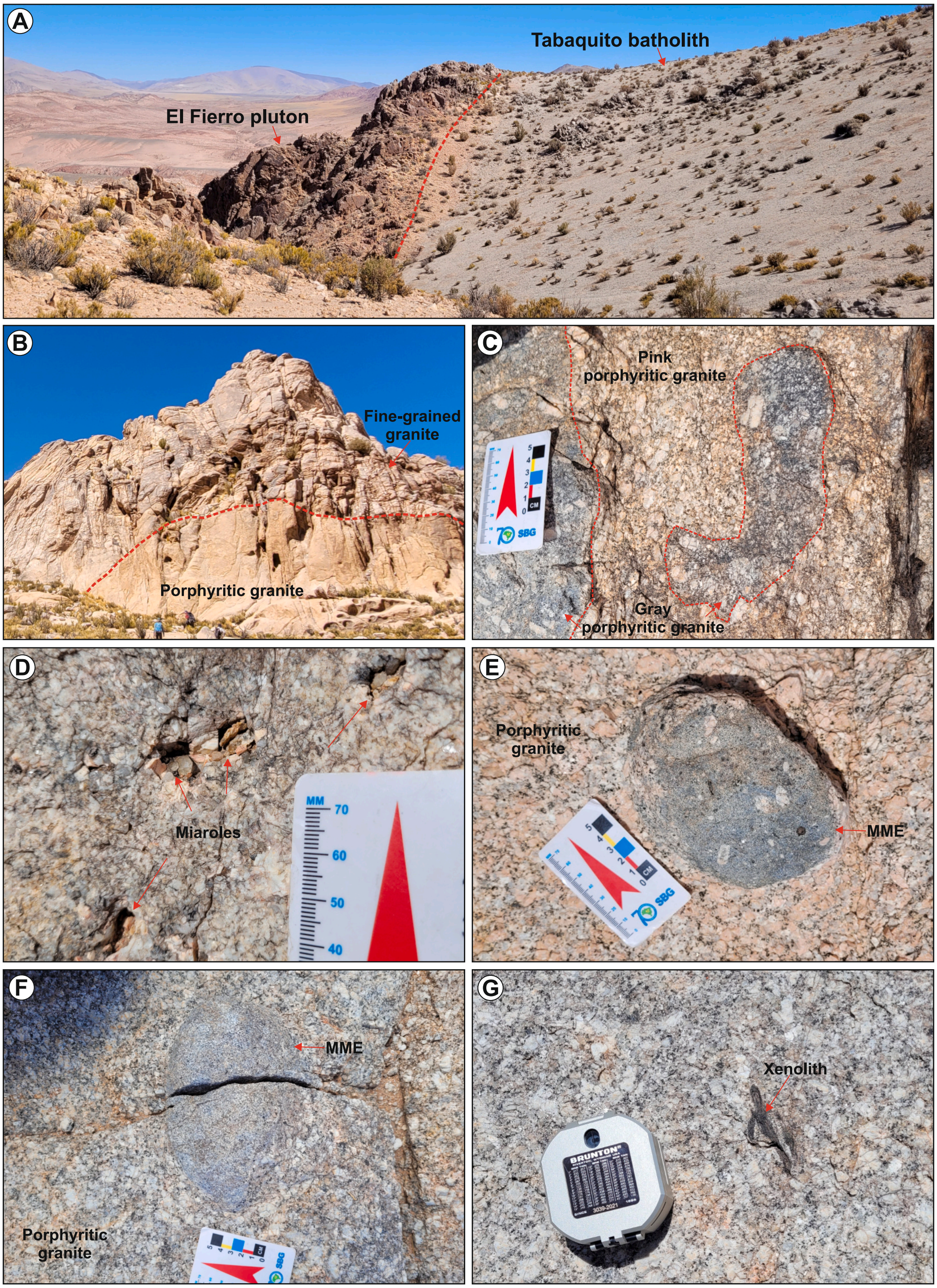

Fig. 3. Field photographs. A) Sharp contact between the Tabaquito granodiorite and the El Fierro pluton. B) Outcrop showing the contact between fine- to medium-grained equigranular granites (FM-EG) and medium- to coarse-grained porphyritic granite (CM-PG). C) Contact between domains within the CM-PG facies, where the fine-grained matrix shows a grayer tone compared to the coarse-grained domain. D) CM-PG facies with abundant miarolitic cavities. *E*-F) Ellipsoidal mafic microgranular enclaves (MMEs) with sharp boundaries hosted in the CM-PG facies. G) Centimeter-scale xenolith enclosed in the CM-PG facies.

stage, which clearly point to a calc-alkaline I-type affinity for these granites as indicated by Llambías and Sato (1995).

The studied samples are high silica granites (69.9–76.7 wt% SiO_2) with 11.2–14.7 wt% Al_2O_3, 0.93–3.22 wt% FeO, and low MgO (0.09–0.65 wt%) and TiO_2 (0.10–0.48 wt%). The FM-EG facies shows the lowest MgO and TiO_2 values (0.01 wt% MgO and 0.02 wt% TiO_2).

Chondrite-normalised REE patterns of the El Fierro granites are variably enriched in LREE compared to HREE (La_N/Lu_N = 4.74–39.4; Table 3) (Fig. 10), with the exception of the FM-EG that shows an almost flat pattern relatively enriched in HREE (La_N/Lu_N = 0.86) (Fig. 10). All samples show a strong negative Eu anomaly (Eu/Eu* = 0.05–0.24; Table 3) (Fig. 10). Silicate Earth normalised trace-element patterns are enriched in incompatible elements showing significant troughs in Ba, Nb—Ta, Sr, P and Ti, as well as a variable and large spike in Pb (Fig. 10).

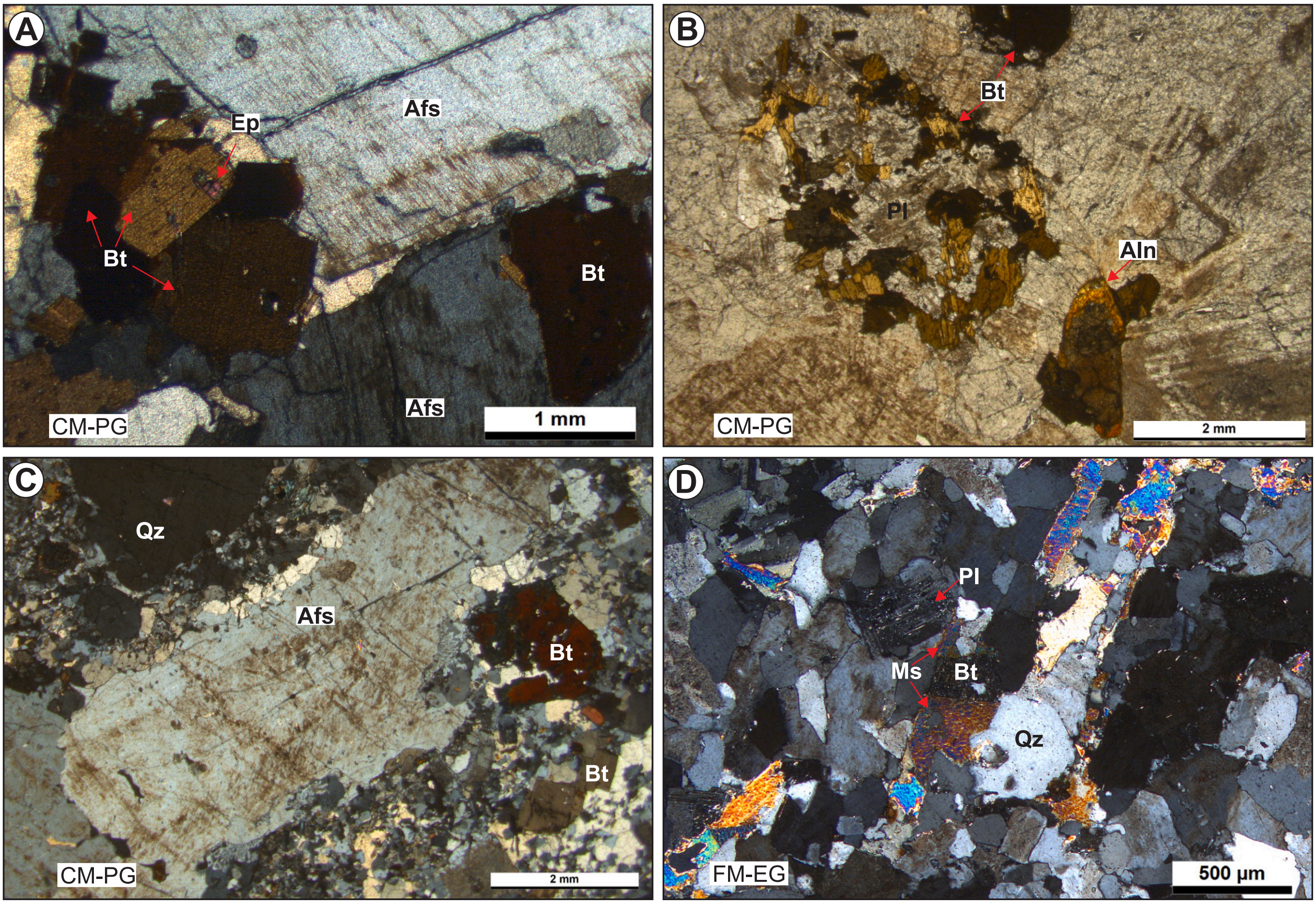

Fig. 4. Photomicrographs of the two facies of the El Fierro pluton. A-C) Medium- to coarse-grained porphyritic granite (CM-PG). In (C), the finer-grained matrix highlights textural variation within the CM-PG facies. D) Fine- to medium-grained equigranular granite (FM-EG). Mineral abbreviations after Whitney and Evans (2010).

8.1. Zircon and apatite saturation temperatures

Apatite-saturation temperatures (T_{Ap}) have been calculated following the thermometric expression developed by Harrison and Watson (1984), based on melt composition (SiO_2 content) and the distribution coefficient of P between apatite and melt (D_P). Correction proposed by Bea et al. (1992) for peraluminous compositions has been applied on samples with ASI ≥ 1, to avoid the effect of the elevated solubility of apatite in peraluminous granitic melts.

Zircon-saturation temperatures (T_{Zr}) have been calculated according to the Watson and Harrison (1983) thermometric expression based on the distribution coefficient of Zr between zircon and melt (D_{Zr}) and parameter M [(Na + K + 2Ca)/(Al Si)] that consider the influence of magma composition on zircon solubility.

The studied samples from the El Fierro pluton have moderately high T_{Zr} of 775 ± 45 °C (range: 717–840 °C; Table 3) with the sample of the FM-EG (TAB-29) showing the lowest temperature (691 °C). The calculated T_{Ap} are high (av. 887 ± 78 °C) with values as high as 993 °C and only two samples showing values below 800 °C (range: 758–993 °C; Table 3). The lowest T_{Ap} is again displayed by sample TAB-29 (665 °C), which is indicative of its more evolved nature. These temperatures are consistent with those obtained for the El Fierro pluton (av. $T_{Ap} = 862 \pm 31$ °C; av. $T_{Zr} = 811 \pm 10$ °C) and the Los Puentes pluton (av. $T_{Ap} = 823 \pm 36$ °C; av. $T_{Zr} = 796 \pm 20$ °C) from data reported by Llambías and Sato (1995), also supporting a relatively high temperature for these magmas.

9. Nd and Sr isotopes

Sr and Nd isotope compositions of the studied samples (TAB-21, TAB-29 and TAB-76) are listed in Table 4. Initial radiogenic isotope ratios were calculated at the crystallisation age of 262 Ma obtained here. Nd model ages (T_{DM}) were calculated with respect to the depleted mantle according to DePaolo et al. (1991). The $^{147}Sm/^{144}Nd$ ratios in samples TAB-21 and TAB-76 are below the threshold value of 0.165, above which calculated model ages tend to be unreliable (see discussion by Stern, 2002). Although sample TAB-29 has a $^{147}Sm/^{144}Nd$ ratio of 0.255, its model age is very similar to those obtained for the other two samples.

The granites of the El Fierro pluton have very uniform εNd_i values ranging between −3.31 and − 3.16 with Nd model ages that vary between 1294 and 1307 Ma (Table 4). The $^{87}Sr/^{86}Sr_i$ ratios are more heterogeneous with values of 0.71633, 0.77061 and an anomalous value of 0.60937 (sample TAB-76) (Table 4). This anomalous value may indicate that the Rb-Sr system was affected by remobilization of both Rb and Sr caused by deuteric alteration as commonly reported in alkaline granites (Montero et al., 2009). The obtained $^{87}Sr/^{86}Sr_i$ values are higher than that reported by Llambías and Sato (1995) from a whole-rock isochron (0.70544 ± 0.00064).

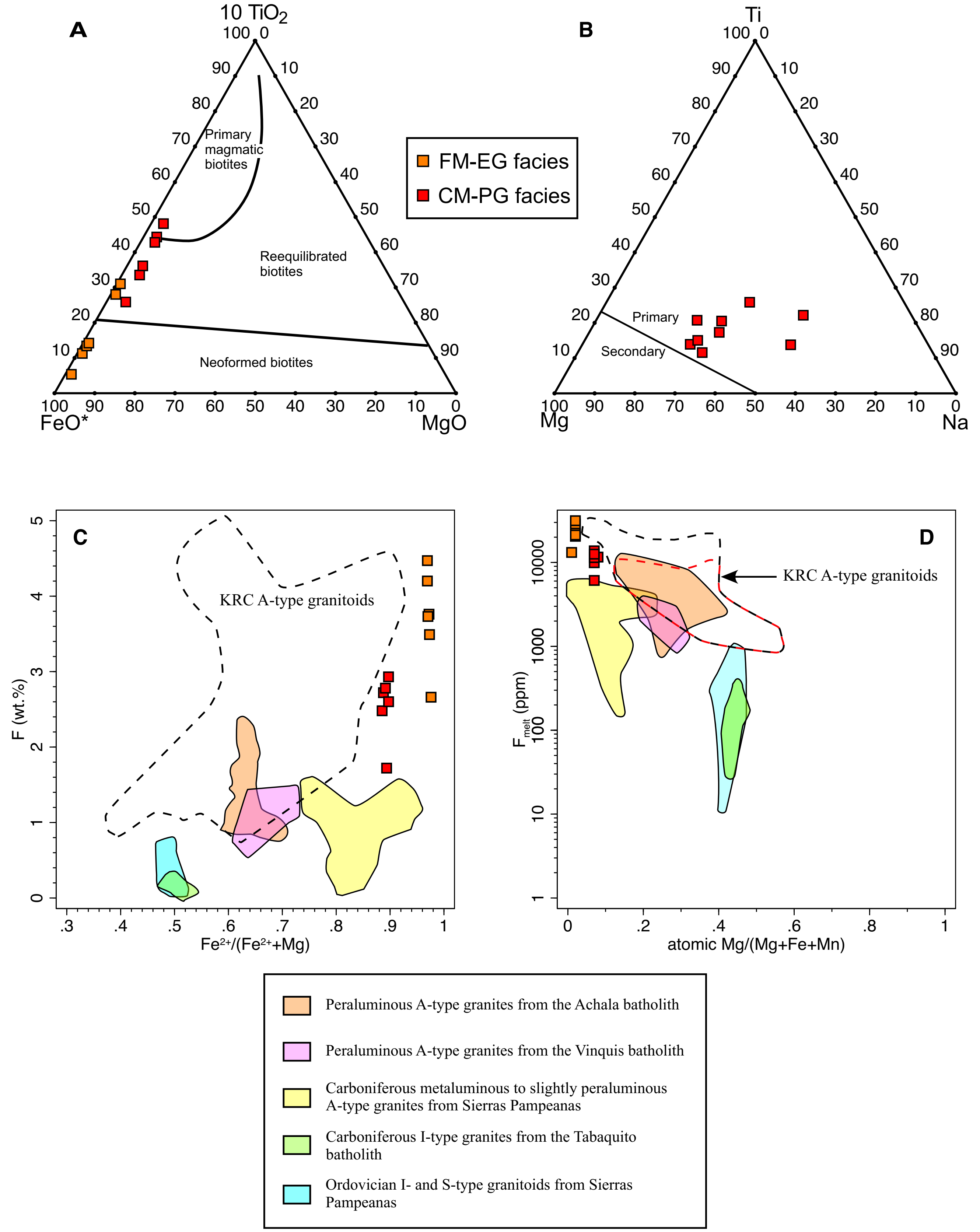

Fig. 5. Composition of micas from the El Fierro granitoids. A) 10 TiO_2–FeO–MgO ternary diagram from Nachit et al. (2005). B) Atomic Ti–Na–Mg diagram with compositional fields for primary and secondary micas from Miller et al. (1981). C) F vs. $Fe^{2+}/(Fe^{2+}+Mg)$ diagram for biotites from this study and from Early Ordovician and Early Carboniferous calcalkaline granites, and metaluminous and peraluminous A-type granites of Sierras Pampeanas, as well as, mataluminous, aluminous and peralkaline A-type granites of the KRC. D) Atomic Mg/(Mg + Fe + Mn) vs. calculated F diagram. F contents have been calculated using the equations of Muñoz (1984, 1992). KRC: Katerina Ring Complex (southern Sinai, Egypt; Moreno et al., 2014).

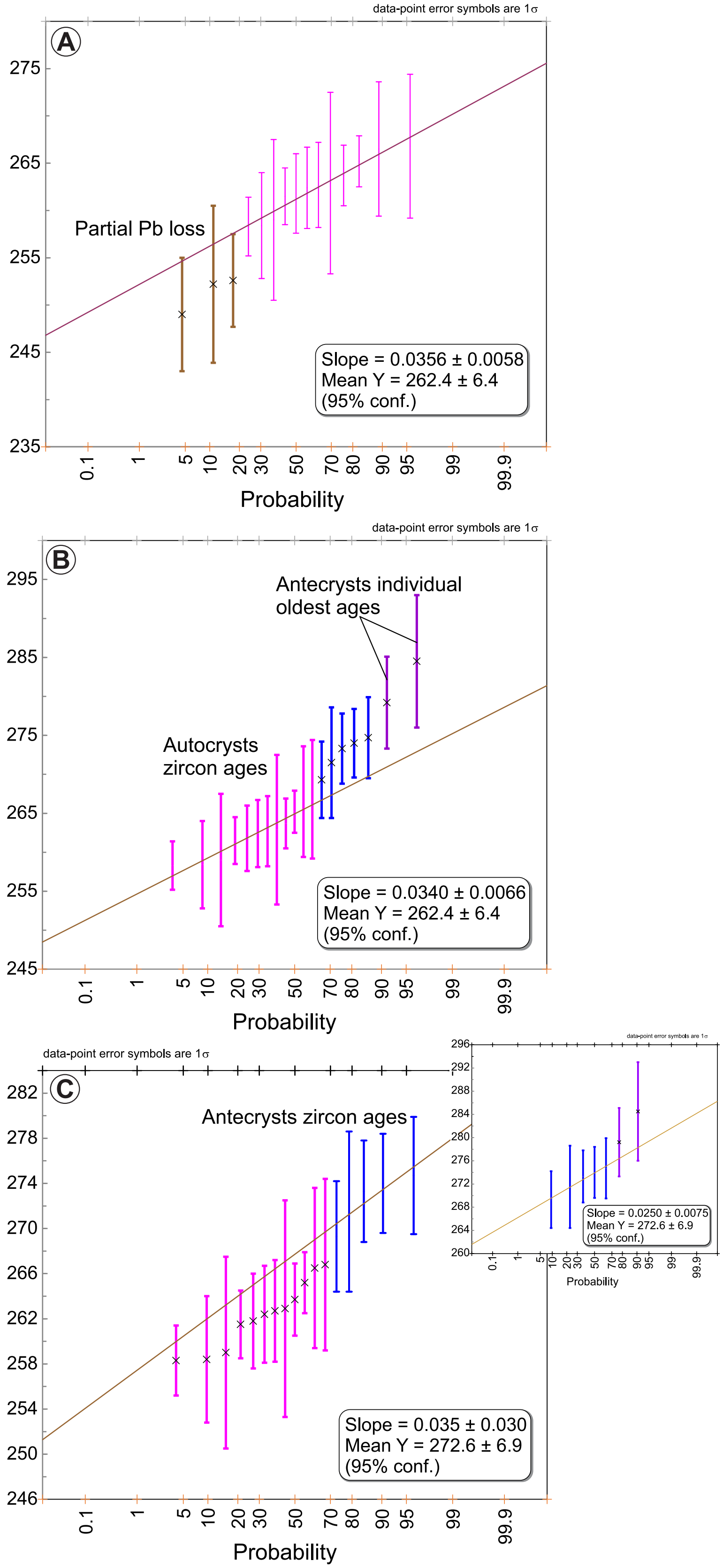

Fig. 6. Linearized probability plots using individual zircon U-Pb ages from the analyses included in Supplementary Material S1 for sample TAB-21. Three age populations are recognized: (A) individual zircon ages assuming partial Pb loss, (B) individual autocrysts zircon ages, and (C) individual antecrysts zircon ages. *Insets:* slope line regression and calculated age. Any data points that deviate from the calculated regression line are excluded. Inset in C): note that two individual antecrysts zircon ages shown in B) are excluded because they deviate from the calculated regression line.

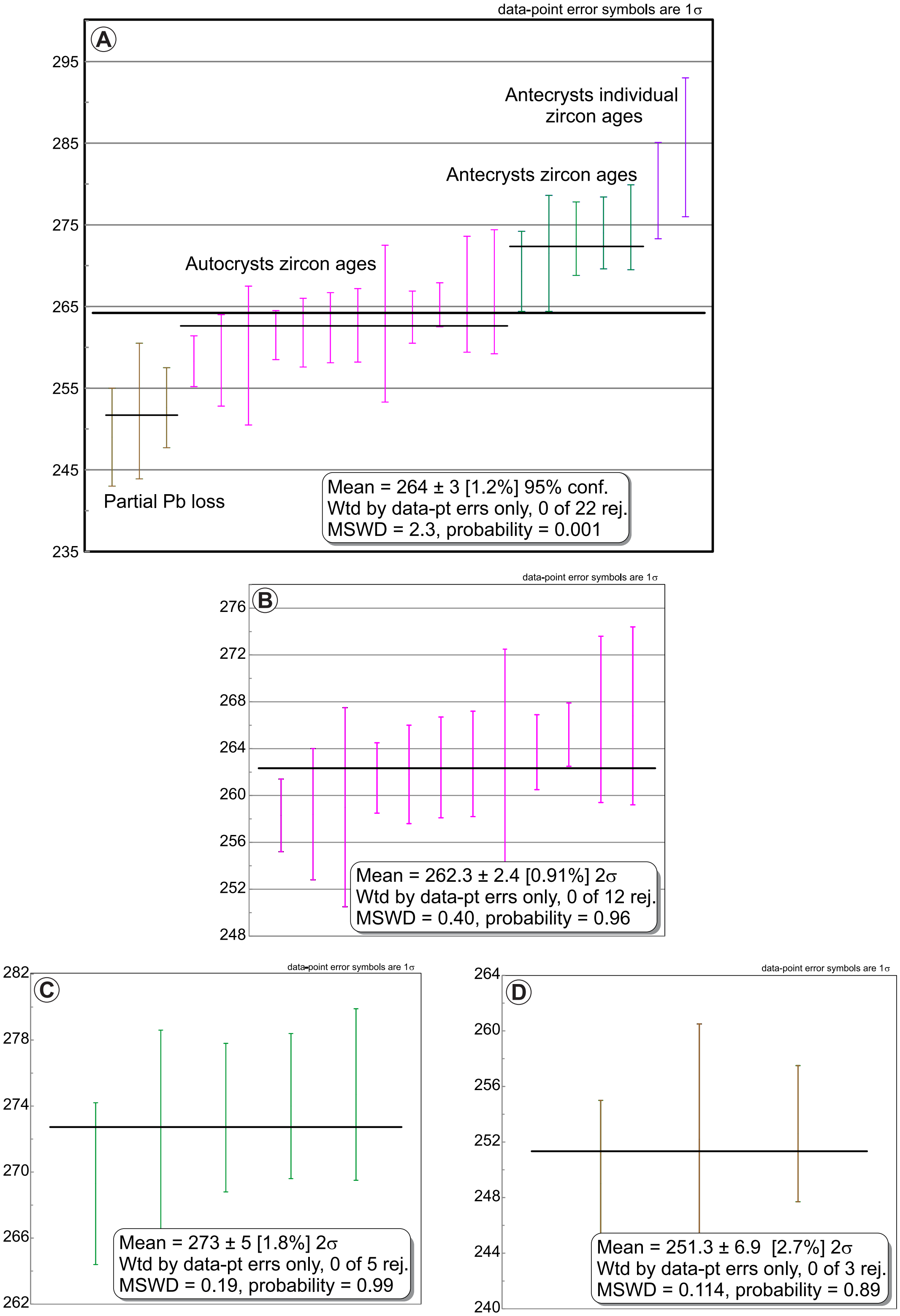

Fig. 7. Weighted mean ages diagrams using individual zircon U-Pb ages from the data projected in Fig. 8. (A) Considering the whole dataset, the samples yield an age with a moderately high MSWD value of 2.3. (B–D) Conversely, the three populations previously distinguished yield ages with lower MSWD values.

10. Discussion

10.1. Geochronology of the El Fierro pluton

Llambías and Sato (1995) reported the first geochronological data of rocks from the El Fierro pluton, obtaining a Rb-Sr whole-rock isochron of 274 ± 3 Ma and Rb-Sr whole-rock and biotite isochrons of 257 ± 1 and 256 ± 1 Ma, as well as Rb-Sr whole-rock and biotite isochron ages of 249 ± 1 Ma and 257 ± 1 Ma for the Los Puentes pluton, a granitic unit comparable to the El Fierro pluton. It should be noted that when reproducing the Rb-Sr whole-rock isochron we obtain an age of 274 ± 12 Ma with a high MSWD of 3.9, so it is an errorchron likely with no

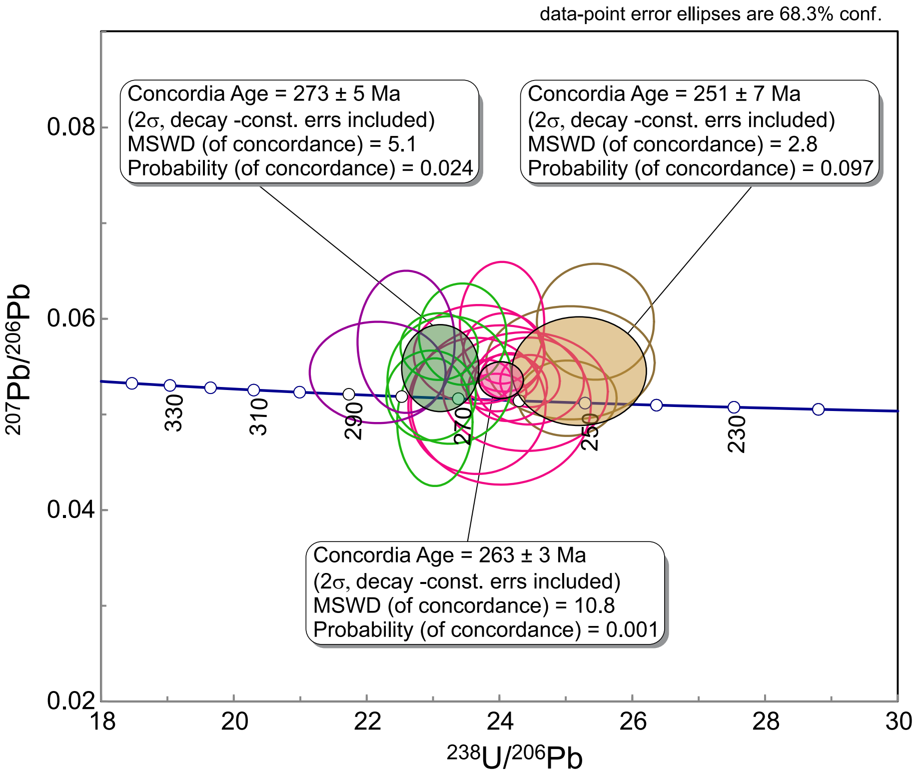

Fig. 8. Tera-Wasserburg Concordia diagram showing the calculated age for sample TAB-21. *Inset* shows the calculated mean ages. Tera-Wasserburg Concordia diagram show recognized age populations. It is known that fitting to the Concordia curve can be poor for ages younger than ca. 400 Ma, where the ^{207}Pb/^{206}Pb ages are extrapolated nearly parallel to the Concordia curve. Thus, small variations in ^{207}Pb can lead to significant dispersion (i.e., high MSWD values). In this case, weighted mean ages using ^{238}U/^{206}Pb are preferable.

geological meaning. Subsequently, Sato et al. (2015) reported a Permian age for a granite sample from the Conconta pluton, which is also equivalent to the El Fierro pluton, using LA-MC-ICP-MS U-Pb zircon data. They found two age populations of 253 ± 2 Ma and 262 ± 2 Ma, whose interpretation is discussed below.

Here we report the first U-Pb zircon age for the El Fierro pluton, also obtaining a Permian age with moderately high MSWD (264 ± 3 Ma, MSWD = 2.3) for this pluton. As mentioned above, this U-Pb zircon age is calculated from a broad range of ages (258–285 Ma) that lacks clear geological significance. This dispersion is inconsistent with evidence suggesting that crystallisation of an average pluton typically occurs in periods significantly shorter than 1 million years (Glazner et al., 2004; Dahlquist et al., 2024c). Conversely, recent works have discriminated distinct age populations, indicating that zircons crystallised from a deep mush reservoir, where prolonged magmatic activity permitted the extended crystallisation of zircon antecrysts. Subsequent migration of the parental magma from the mush reservoir occurred close to the time of emplacement and culminated in the formation of an ephemeral shallow-level magma chamber, where zircon autocrysts crystallised (Lim et al., 2023; Dahlquist et al., 2024c; Santos da Cruz et al., 2024). Following this conceptual model, we postulate the existence of zircon antecrysts (273 ± 5 Ma, $n = 5$) and autocrysts (262 ± 2 Ma, $n = 12$) within a long-lived magmatic system, the latter defining the emplacement crystallisation age, together with a younger zircon population (251 ± 7 Ma, $n = 3$) that was probably affected by partial Pb loss (see Section 6). Notably, the ages of 262 ± 2 Ma (autocrysts) and 251 ± 7 Ma (zircon affected by Pb loss) are the same that those reported by Sato et al. (2015) for the Conconta pluton (262 ± 2 Ma and 253 ± 2 Ma), although the interpretations are contrasting. Sato et al. (2015) interpret the younger age as the crystallisation age of the pluton, but the five zircon ages used in the calculation are highly discordant with the most concordant datum being only 87% concordant. Therefore, this supports the argument about the younger age representing zircon grains affected by partial Pb loss. Furthermore, this in turn partly resolves the controversy found by Sato et al. (2015) with the ages of the Conconta and Chita plutons, since regarding the magmatic stratigraphy described by Llambías and Sato (1990) the Chita pluton (260 ± 5 Ma) should not be older than the Conconta pluton. On the other hand, it is well established that Rb-Sr ages are generally younger than U-Pb zircon ages, as the Rb-Sr system closes at a relatively low temperature (ca. 400 °C) and is susceptible to modification (e.g., Jenkin et al., 2001). So, the ages of 256 and 257 Ma reported by Llambías and Sato (1995) are comparable to the younger age of 251 Ma obtained in this study and support the interpretation that this younger age does not represent a crystallisation age. Consequently, the U-Pb zircon age of 262 ± 2 Ma represents the best estimate of the crystallisation age of the El Fierro and Conconta plutons.

Interestingly, the older age of 273 ± 5 Ma, possibly representing zircon antecrysts, suggests that magmatic activity may have begun around 273 Ma. In this case, the beginning of the magmatism that gave rise to the late-stage plutons of the Choiyoi group (ca. 265–252 Ma; Rocher et al., 2024), took place earlier than previously thought at ca. 273 Ma. Therefore, the magmatic system would have started around 273 Ma and would overlap with the youngest ages of the early-stage plutons (ca. 285–272 Ma; Rocher et al., 2024) of the Choiyoi Magmatic Province. Similarly, the early-stage magmatism is interpreted to have started around 290 Ma, with emplacement occurring at ca. 278 Ma, based on U-Pb zircon dating of the Cerro Punta Blanca pluton (Dahlquist et al., 2024a).

Alternatively, this older age (ca. 273 Ma) may represent zircon xenocrysts entrapped during the intrusion and emplacement of these granites, since the El Fierro pluton intrudes the Las Piedritas pluton (not dated so far) which is likely equivalent to the Los Leones, Agua Negra and Tocota plutons (Llambías and Sato, 1995; Sato et al., 2015) with ages of 279 ± 4 Ma (Los Leones pluton), 272 ± 2 Ma (Agua Negra

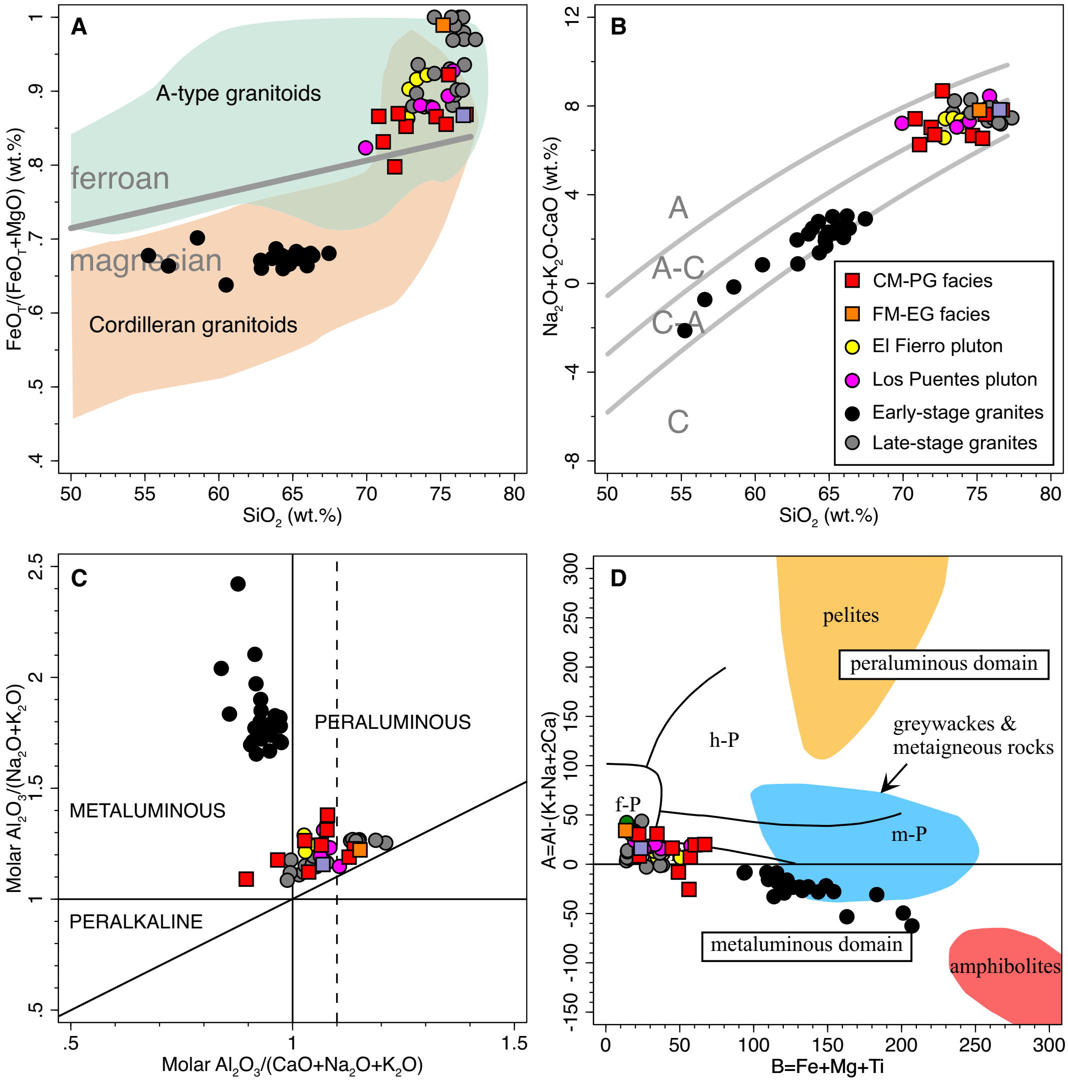

Fig. 9. Whole-rock composition of the granitoids from the El Fierro pluton along with other plutons of the Colagüil batholith. A) Fe-number vs. SiO_2 diagram. A-type and Cordilleran granitoid fields after Frost et al. (2001). B) MALI-index vs. SiO_2 diagram after Frost et al. (2001). C) Molar alumina saturation index vs. Al_2O_3/(Na2O + K_2O). D) A-B diagram after Debon and Le Fort (1983), modified by Villaseca et al. (1998). l-P, low peraluminous; m-P, moderately peraluminous; h-P, highly peraluminous; f-P, felsic.
peraluminous suites.

pluton) and 280 ± 4 to 274 ± 2 Ma (Tocota pluton) (Sato et al., 2015; Jones et al., 2015; Poole et al., 2020). Nonetheless, this hypothesis seems less probable, because of the distinctive and contrasting compositions of each magmatic event and because there is no field evidence of interaction or assimilation (e.g., enclaves from the early-stage granites). If the older ages (269–275 Ma) that yield the 273 Ma age represent magmatism of the early-stage Choiyoi plutons, other populations of older ages should be present. As demonstrated by Dahlquist et al. (2024a), early-stage Choiyoi granites record ages ranging between ca. 277 and 290 Ma, with several ages clustering between 279 and 291 Ma (n = 12 out of 20 analyses from the dated sample). High proportions of these ages in the early-stage Choiyoi granites, have also been reported in other studies (e.g., Sato et al., 2015) and in our own unpublished data, but they are mostly absent in the present work. In this context, the older two ages of 279 and 285 Ma could be interpreted as antecrystic rather than xenocrystic zircon, although further data are needed to support a more robust conclusion.

10.2. Characterisation and classification of the El Fierro pluton

The granites of the El Fierro pluton are ferroan, alkali-calcic to calc-alkalic, and alkaline (Figs. 9 and 11) in the sense of Sylvester (1989), who grouped together A-type granites and highly fractionated calc-alkaline and alkaline granites under the term “alkaline”. They also share these characteristics with rocks of the Los Puentes pluton and the other late-stage plutons of the Colangüil batholith (Figs. 9 and 11) and being certainly different from the early-stage plutons with strong calc-alkaline I-type affinity (Fig. 9). Consistently, most samples show high Ga/Al ratios (Fig. 11) and relatively high concentrations of HFSE and LREE (yielding smooth REE patterns with a significant negative Eu anomaly), as well as variable and ranging to high Nb and Ce contents (Supplementary Material S7), which are characteristic of A-type granites (e.g., Whalen et al., 1987; Eby, 1990; Bonin, 2007; Dahlquist et al., 2010). This is also supported by the mineralogy of the El Fierro pluton with quartz, oligoclase to albite plagioclase and K-feldspar as felsic minerals and siderophyllite as the main mafic mineral, as well as accessory allanite and fluorite (Llambías and Sato, 1995). The high F content of the biotite and the very high calculated F content of the melt

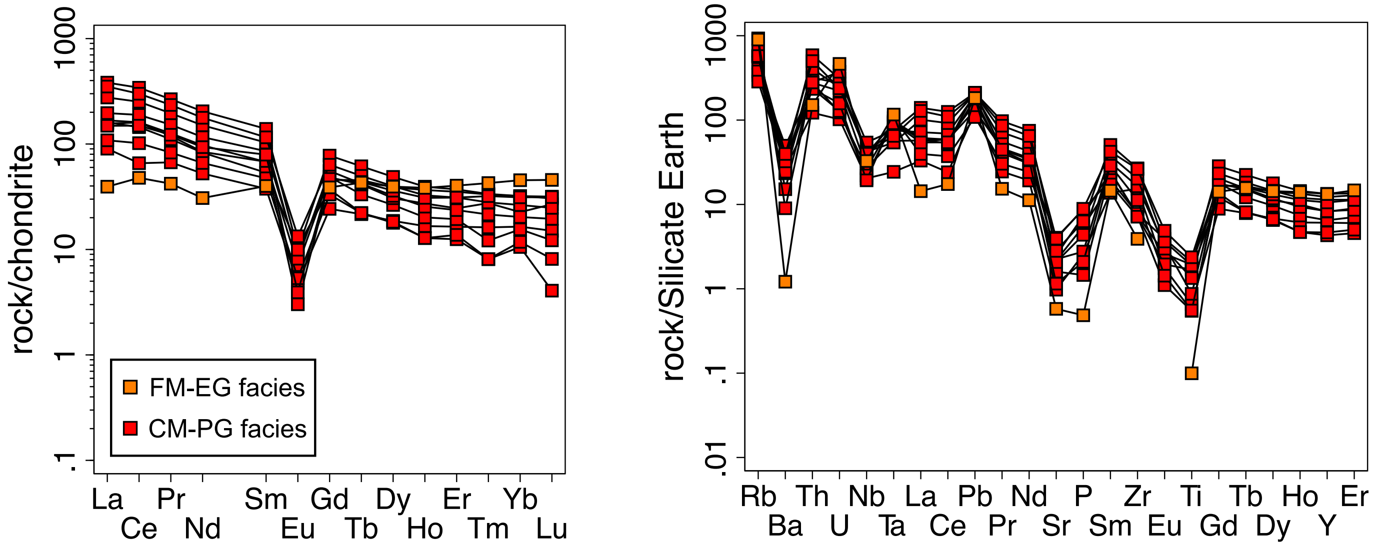

Fig. 10. Chondrite-normalised REE and Silicate Earth-normalised trace element diagrams. Normalisation values after McDonough and Sun (1995).

(Supplementary Material S5), together with the high T_{AP} and T_{Zr}, are also typical of A-type granites (mostly >740 °C; e.g., King et al., 2001; Dahlquist et al., 2010; Moreno et al., 2014, 2017; Gao et al., 2017). Accordingly, both samples from the El Fierro pluton and those from the late-stage granites plot in the field of within-plate granites in the tectonic discriminating diagrams of Verma et al. (2013) (Fig. 12A), reinforcing their A-type signature.

The $FeO_T/(MgO + FeO_T)$ ratio vs. Al_2O_3 diagram (Fig. 12B) of Dall'Agnol and Oliveira (2007) allows to classify most samples from the El Fierro pluton as oxidized A-type granites with the exception of the more evolved FG-MG facies that plot as reduced A-type granites along with other samples of the late-stage granites (Fig. 12B). A-type granites, ranging from reduced to oxidized conditions, are well documented in the geological literature (Dall'Agnol et al., 2017). On the other hand, the early stage-granites are obviously classified as calc-alkaline granites (Fig. 12B).

Therefore, the late-stage plutons of the Colangüil batholith may be classified as A-type granites, since most of them share geochemical traits, although further work is needed, and the early-stage plutons as I-type granites, as suggested by Llambías and Sato (1995). This is also consistent with the interpretation by Rocher et al. (2024), which suggests that early-stage plutonic magmatism of the Choiyoi Magmatic Province, with calc-alkaline I-type affinity, developed between ca. 285 and 272 Ma and was followed by the late-stage plutons with an A-type signature around ca. 265–252 Ma.

10.3. *Assessment of the source and petrogenesis of the A-type granites*

The genesis of A-type granites remains a subject of ongoing debate, with potential origins including fractional crystallisation of mantle-derived magmas, partial melting of the lower crust, or mixture of these two endmembers (see Bonin, 2007, for further details). All samples from the late-stage plutons of the Colangüil batholith plot as A_2-type granites in the discriminating diagrams of Eby (1992) (Fig. 13A, B),

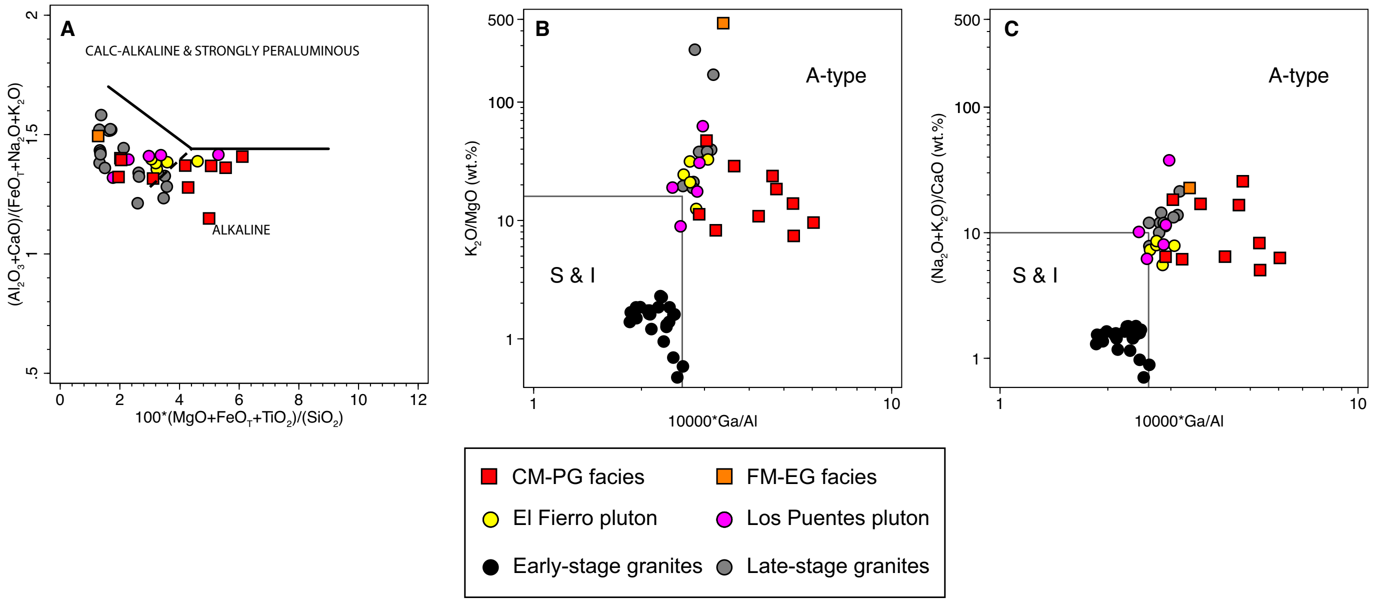

Fig. 11. A) Granite discrimination diagram of Sylvester (1989) for the late-stage granites of the Colangüil batholith. The dashed line separates alkaline granites whose compositions resemble highly fractionated calc-alkaline granites from those that do not. B–C) Granitoids discrimination diagrams from Whalen et al. (1987) for the granites of the Colangüil batholith.

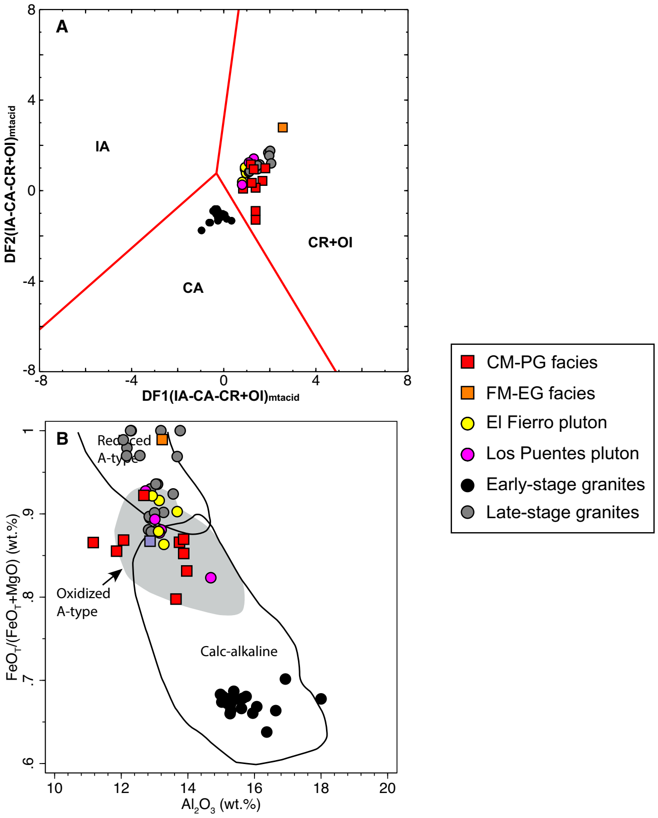

Fig. 12. A) Multidimensional discrimination diagram based on long-transformed ratios of the major-trace elements for tectonic discrimination of the granites from the Colangüil batholith. Discriminant-function equations for this diagram are detailed in Verma et al. (2013). Abbreviations: CR + OI–Continental rift + Ocean Island, Col–Collision, IA–Island arc, CA– Continental arc. B) Whole-rock $FeO_T/(FeO_T + MgO)$ vs. $Al_2O_3/(K_2O/Na_2O)$ diagram with compositional fields for reduced A-type, Oxidized A-type and calc-alkaline granites after Dall'Agnol and Oliveira (2007).

which indicates an affinity with continental crust or sources modified by subduction-related processes. A few samples of the El Fierro pluton plot on the boundary between A_1- and A_2-type granites (Fig. 13A, B). Accordingly, all samples from the Colangüil batholith match the composition of A_2-type granites in the diagram of Moreno et al. (2016) (Fig. 13C). Consequently, these A-type granites exhibit trace element ratios comparable to either continental crust or subduction-related magmatic sources (Eby, 1990, 1992; Moreno et al., 2014, 2016).

The relationships between $(Ce/Pb)_N$ and $(La/Nb)_N$ ratios (Fig. 13D) may indicate crystal fractionation of LREE accessory minerals such as allanite (e.g., Moreno et al., 2014, 2016), which is corroborated by the compatible character of the LREE suggested by positive correlations of $(Ce/Pb)_N$ and $(La/Nb)_N$ with Zr/Hf (Supplementary Material S7) and by the more prominent positive Pb anomaly displayed by the more evolved samples (Fig. 10). This apparent enhancement of the Pb anomaly can be explained by the preferential incorporation of LREE into allanite during fractionation, which significantly reduces LREE concentrations while Pb contents remain nearly constant, resulting in a more pronounced Pb anomaly and lower Ce/Pb ratios in evolved compositions (e.g., Rowe et al., 2007; Moreno et al., 2016).

Regarding Nd and Sr isotope compositions, the negative εNd_i values of ca. −3 with Nd model ages around 1400 Ma, along with the high $^{87}Sr/^{86}Sr_i$ ratios (0.71633 and 0.77061) of the El Fierro pluton point to a significant crustal component in the source of these magmas, although the $^{87}Sr/^{86}Sr_i$ ratio of 0.70544 reported by Llambías and Sato (1995) may indicate the involvement of a mantle component or a heterogenous continental crust at the source level. However, the $^{87}Sr/^{86}Sr_i$ ratio must be considered with care, since the Rb/Sr system shows signs of partial disturbance, as previously discussed.

The variable range of εHf_t obtained for different zircon grains in one sample of the coarse-grained porphyritic facies (−7.0 to +1.25; $n = 13$) with predominance of negative values (−7.0 to −1.28; $n = 9$) also highlight an important crustal imprint, although with minor participation of a mantle-derived source or a heterogeneous crust as suggested by positive and slightly negative values (−0.82 to +1.25; $n = 4$). In addition, although mantle-derived magmas may have had only a minor role at the source level, they likely played an important role as a heat source for the late-stage granitic magmatism.

Interestingly, similar values of εHf_t have been reported for plutons of the early-stage of the Choiyoi group: 1) the Cerro Punta Blanca pluton from the Frontal Cordillera of Mendoza with an emplacement crystallisation age of 278 Ma and εHf_t that varies between −8.93 and + 0.17 (Dahlquist et al., 2024a); 2) the Tocota pluton from the Colangüil batholith with a crystallisation age of ca. 280–274 Ma for which contrasting data have been reported with εHf_t ranging between −1.9 and + 0.5 (Poole et al., 2020) and between +1.5 and + 3 (Jones et al., 2015). Although more isotopic data are needed, this might suggest that isotopically similar sources were involved in the generation of both the early-stage calc-alkaline magmatism and the late-stage A-type magmatism.

Hf isotopic variability in metaluminous to slightly peraluminous systems have been explained through open system processes (e.g., hybridisation, assimilation, metasomatism) or heterogenous sources (e.g., Kemp et al., 2007; Teixeira et al., 2011; Moreno et al., 2020; Dahlquist et al., 2023, 2025; Lim et al., 2023).

It is worth noting that the εHf_t values in the studied sample are independent of the zircon age, something that has also been recorded in the Permian Cerro Punta Blanca pluton from the Frontal Cordillera of Mendoza (Dahlquist et al., 2024a). Recently, Dahlquist et al. (2025) have indicated that Hf isotopic variability within the same sample and with no age correlation may be indicative of a heterogeneous source but also of a highly heterogenous deep mush reservoir in a long-live magmatic system. A situation that may have occurred in the El Fierro pluton if we consider the age of ca. 274 Ma as antecrysts incubated in a deep mush reservoir.

Contrary to the isotopic similarities between the early-stage and the late-stage granites described above, we can infer certainly different sources for both groups of granites considering their major elements compositions (Fig. 14). Thus, the late-stage granites such as those from the El Fierro pluton show notable affinity with metasedimentary sources (Fig. 14), which is also supported by biotite chemistry (Supplementary Material S4) and the presence of primary muscovite, whereas the early-stage granites show a strong affinity with K-rich mafic sources (Fig. 14).

When applying the approach described by Bea et al. (2018) to calculate T_{DM} values, the resulting Hf T_{DM} values are much higher than the calculated two-stage Hf T_{DM} values (see Section 7). This discrepancy is possibly due to the fact that the model of Bea et al. (2018) considers the Lu/Hf ratio of the source itself (i.e., a source composed of continental crust including metasediments), rather than the commonly assumed present-day Lu/Hf value for the continental crust used in the two-stage T_{DM} calculations. Thus, these very high T_{DM} values are indicative of heterogenous continental crust including metasediments in the source leading to non-realistic T_{DM} values. The lack of a substantial detrital zircon population is likely attributable to the analyses being focused on the magmatic growth rims of the zircon as indicate in Section 6. However, zircon morphology described in Section 6, indicates a possible origin from a heterogeneous source, such as metasediments.

In addition, the classification of many samples of the late-stage granites as reduced A-type granites (Fig. 12B) could be due to the reduced character of the source or the contribution of a metasedimentary source (Dall'Agnol and Oliveira, 2007). According to this, biotite chemistry of the studied samples also indicates reduced conditions or a metasedimentary affinity, since it has Fe/(Fe + Mg) ratios typical of rocks of the ilmenite series (Supplementary Material S4). All of

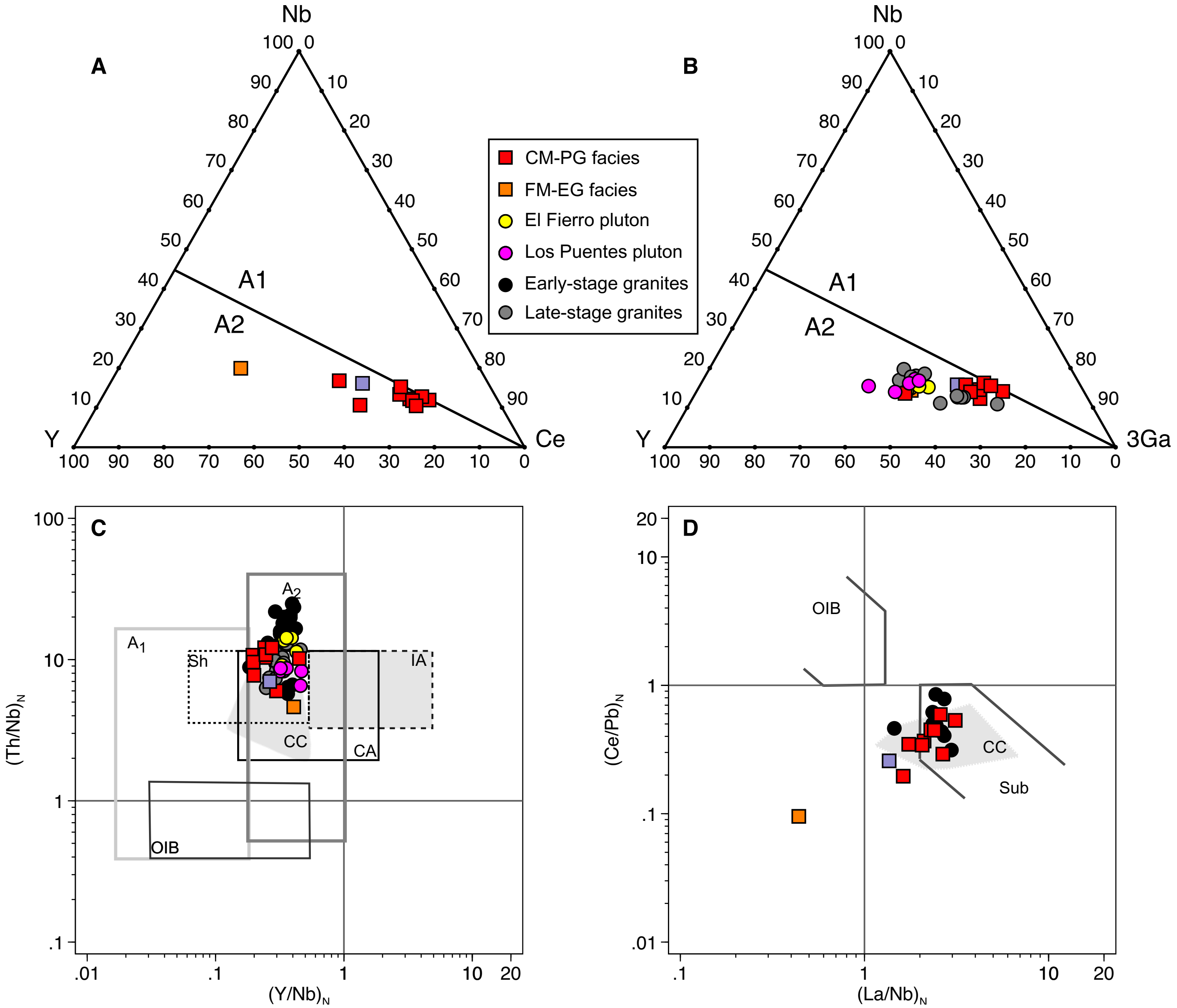

Fig. 13. A-B) A-type granitoids discrimination diagrams of Eby (1992) for the granites of the Colangüil batholith. C–D) Relationships between Y/Nb, Th/Nb, La/Nb and Ce/Pb in the granoids from the Colangüil batholith. Normalisation values after McDonough and Sun (1995). Compositional fields after Moreno et al. (2016). Abbreviations: A$_1$, A$_1$-type granitoids; A$_2$, A$_2$-type granitoids; CA, Continental Arcs; CC, Continental Crust; IA, Island Arcs; OIB, Ocean Island Basalts; Sh, shoshonites; Sub, subduction-related magmatic suites.

this therefore highlights significant differences at the source level between the two groups of granites, that is the early-stage and late-stage plutons of the Choiyoi Group.

Based on Hf isotope data from zircon, Dahlquist et al. (2024c) proposed a heterogeneous continental source for the early-stage plutons in the Frontal Cordillera of Mendoza. Similar Hf isotope data from zircon reported here for the El Fierro pluton suggest a comparable source, although the geochemistry and mineral chemistry indicate the involvement of metasedimentary material in the source.

Summarizing, both granite groups share characteristics of crustal sources, but the early-stage granites likely derived from a heterogeneous mafic crustal source whereas the late-stage granites likely derived from a crustal source that involved metasedimentary material. As described in Section 10.5, the early-stage plutons originated in an extensional arc setting as a result of an initial oceanic slab rollback process, which was still incipient during the generation of the late-stage plutons. This incipient extensional arc would have favoured a progressive increase in heat, allowing the melting of upper crustal levels containing metasedimentary components with limited mantle contribution.

Finally, the late-stage granites such as the studied El Fierro pluton evolved through fractional crystallisation of feldspars as indicated by the significantly negative anomalies of Eu, Ba and Sr, along with crystal fractionation of biotite and accessory minerals (at least apatite, zircon and allanite). This is also supported by the development of highly evolved cupola-type granites that constitute the marginal facies. Although the detailed physical mechanisms lie beyond the scope of this study, processes such as compaction without deformation of solids ("crystal repacking"; Bachmann and Huber, 2019), previously encompassed within the broader concept of filter pressing, may have contributed to the formation of this marginal fine-grained unit.

10.4. Volatile components of the melt

High halogens content, particularly F, is an intrinsic characteristic of A-type granites (e.g., Collins et al., 1982; Eby, 1992; Charoy and Raimbault, 1994; Dahlquist et al., 2010; Wang et al., 2018). These

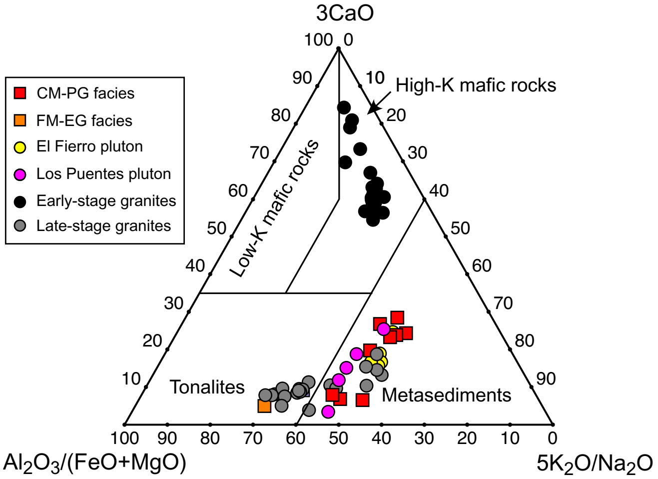

Fig. 14. Ternary $Al_2O_3/(FeOt + MgO)$ – 3CaO – $5(K_2O/Na_2O)$ diagram for discriminating potential sources of granitoids. Compositional fields after Laurent et al. (2014).

halogens play a decisive role in enriching HFSE concentrations in such magmas through the formation of stable complexes (e.g., Keppler, 1993). However, F and Cl are not commonly analysed in igneous rocks; therefore, their concentrations are normally inferred from the measured F and Cl contents of F- and Cl-bearing minerals such as biotite and apatite (e.g., Dahlquist et al., 2010; Moreno et al., 2014; Wang et al., 2018).

The melt halogen contents, calculated from the measured F and Cl concentrations in biotite, indicate that the calculated melt F content for the samples from the El Fierro pluton is very high (6101–31,442 ppm; Fig. 5D; Supplementary Material S5), whereas the calculated Cl content is lower but still relatively high (269–1052 ppm; Supplementary Material S5).

The obtained Cl contents overlap with those reported for the Carboniferous A-type granites of the Sierras Pampenanas (Cl: 90–1050 ppm; Dahlquist et al., 2010) and those reported for the strongly peraluminous A-type granites of the Achala and Vinquis batholiths (Cl: 30–780 ppm; Morales Cámera et al., 2022).

The relatively lower Cl contents compared to F may reflect its preferential partitioning into the aqueous fluid phase during magmatic evolution, as documented in experimental studies (e.g., Webster, 1997; Webster et al., 2009; Keppler, 1993). This behaviour contrasts with fluorine, which remains largely in the melt until late stages, promoting extreme enrichment.

Regarding the F content, the fine-grained granite (FM-EG) exhibits the highest values, only comparable to those of the more evolved granites from the Katerina Ring Complex (Sinai, Egypt, Moreno et al., 2014) (Fig. 5D; Supplementary Material S5), whereas the studied porphyritic granite (CM-PG) matches the higher F values of the strongly peraluminous A-type granites from the Achala and Vinquis batholiths (Fig. 5D) (F: 830–11,260 ppm; Supplementary Material S5) and exceeds those from the Carboniferous metaluminous A-type granites of the Sierras Pampenanas (F: 580–5600 ppm; Dahlquist et al., 2010) (Fig. 5D). Moreover, the studied granites show higher Cl contents (with partial overlap) and significantly higher F contents than those from the Carboniferous arc-related I-type granites from the Frontal Cordillera ($F \leq 355$ ppm; Cl: 250–630 ppm; data from Moreno et al., 2020; see Supplementary Material S5) and those from the I- and S-type granites of Sierras Pampeanas ($F \leq 960$ ppm; $Cl \leq 250$ ppm; data from Dahlquist et al., 2010 and Zandomeni et al., 2021). These contrasts reflect fundamental differences in parental magma sources (cf. Dahlquist et al., 2010), consistent with Wang et al. (2018), who documented similar halogen variations between spatially associated I- and A-type granites in South China, and with the general halogen-rich character of the A-type granites (e.g., Collins et al., 1982; Eby, 1990).

The F-rich signature of the late-stage granites of the Colangüil batholith is also supported by occasional fluorite in the El Fierro and Las Opeñas plutons and by abundant accessory fluorite and fluorite veins in the Agua Blanca and Chita plutons (Llambías and Sato, 1995).

High F contents in A-type magmas have been explained by halogen and alkali rich fluids originated by mantle degassing (Bailey, 1980) causing metasomatism of the crust (Martin, 2006) or through the breakdown of halogen rich biotite and amphibole in the lower crust (e.g., Collins et al., 1982; Skjerlie and Johnston, 1993). Consequently, the origin of high halogen contents in A-type granites is controversial and remains unresolved (see discussion in Wang et al., 2018). Furthermore, fluorine usually behaves incompatibly ($Kd < 1$) during anhydrous mineral fractionation (e.g., feldspars), leading to extreme enrichment in residual melts (Christiansen et al., 1984; Landenberger and Collins, 1996; Sallet, 2000; Li et al., 2020). Wang et al. (2018) proposed that the elevated F contents in A-type granites would require a F-rich source and prolonged magma differentiation that would further elevate the F content.

The high estimated F contents of the El Fierro granites are like those from A-type granites formed from crustal/mantle sources metasomatized by F-rich mantle-derived fluids (e.g., Montero et al., 2009; Moreno et al., 2014), such as the Katerina Ring Complex granites (Fig. 5D) and the A-type granites from the Galiñeiro Intrusive Complex (northwest Spain; Montero et al., 2009) (measured whole-rock F = 300 to 7200 ppm), most likely pointing to enrichment at the source level. In addition, the high calculated F along with the presence of scarce fluorite (Llambías and Sato, 1995), would support the experimental model of Li et al. (2020), where fluorite saturation critically depends on the initial F content of the magmatic source and not solely on melt composition (e.g., the abundance of network-modifying cations such as Mg, Ca, Na). However, this hypothesis requires further evaluation through a systematic study of accessory minerals to determine whether the fluorite is magmatic or hydrothermal.

Therefore, the very high F contents in the El Fierro granites, mainly in the FM-EG facies, could be explained by a predominantly metasomatized crustal source, considering that processes involving only crustal anatexis rarely enrich magmas to such high F levels. This is supported by the large number of S-type granites with low F contents (Morales Cámera et al., 2020), as well as by the F-poor leucosomes from metamorphic terranes (Bonin, 2007). Moreover, fractional crystallisation processes further concentrated residual F during late-stage magmatic evolution.

The process of magmatic differentiation, driven by the crystallisation of anhydrous phases, also leads to a significant enrichment of H_2O in the residual melt, as water behaves incompatibly in these minerals (Whitney, 1988). The combined increase in F and H_2O content profoundly influenced the physical properties of the melt during the late stages of evolution. It lowered its viscosity and solidus temperature, promoted volatile saturation, and enhanced the mobility of the residual melt.

The occurrence of marginal aplitic facies in the studied pluton, interpreted as highly evolved cupola granites, is a direct petrological manifestation of this process, as such lithologies typically form from water- and halogen-rich residual melts during advanced fractional crystallisation (Glazner et al., 2020; Cobbing, 2000; London, 2008).

Thus, the halogen-rich nature of the El Fierro granites reflects a combination of source enrichment and late-stage fractionation, consistent with the general characteristics of A-type magmatism.

10.5. Geodynamic scenario

As indicated by Rocher et al. (2024) early-stage plutons (ca. 285–270 Ma) are primarily tonalite-diorite to granodiorite-monzogranite with a calc-alkaline composition. In contrast, late-stage plutons (ca. 265–252 Ma) display syenodiorite and alkali granite compositions. According to Dahlquist et al. (2024a) and Rocher et al. (2015, 2024), early-stage plutons developed in an extensional arc as result of an initial ocean slab rollback process at ca. 290 Ma. Around 265 Ma, the oceanic slab rollback was incipient, with a dominant extensional regime, leading to the development of the late-stage plutons. The likely existence of zircon antecrysts (~273 Ma) might suggest that magmatism began during waning subduction, overlapping with the early Choiyoi stage (ca. 285–272 Ma). Although discussing the mechanisms responsible for the generalised extensional setting is not the aim of this work, it is worth noting that this regional extension has also been attributed to other mechanisms, such as slab break-off (Gianni and Navarrete, 2022).

The A-type signature of the El Fierro pluton (ferroan, mid-alkaline, high F and HFSE contents) aligns with the late-stage Choiyoi magmatism (265–252 Ma) described by Rocher et al. (2024), marking slab retreat and lithospheric thinning.

The exceptionally high F contents (6101–31,442 ppm) would have promoted shallow emplacement by lowering melt viscosity and solidus temperatures (London, 1997), which is consistent with the shallow-level emplacement of these plutons (Rocher et al., 2024 and references therein).

The hybrid isotope signature —evidenced by εHf_t variability (−7.0 to +1.25)—reflects melting of metasediments (dominant negative εHf_t) with limited mantle inputs or a heterogeneous continental crust (positive εHf_t), consistent with the reduced A-type affinity of many Choiyoi late-stage granites and the El Fierro biotite chemistry. This contrasts with earlier I-type suites, highlighting a shift from subduction-modified to crust-dominated sources during extension. This is well observed in Fig. 12A where the early-stage I-type granites plot as arc-related rocks and the late-stage A-type granites as continental rift-related rocks in the tectonic discrimination diagrams of Verma et al. (2013).

The halogen and HFSE abundances of the El Fierro pluton distinguish it from the early-stage plutons of Choiyoi magmatism (Gregori et al., 2013; Dahlquist et al., 2024a) and Carboniferous arc granites (Moreno et al., 2020). These compositional differences likely reflect shifts within a changing geodynamic setting, from an extensional, subduction-related magmatic arc that evolved into a predominantly extensional environment during the latest Permian, in accordance with Dahlquist et al. (2024a) and Rocher et al. (2015, 2024). Here, the A-type magmatism arose from asthenospheric upwelling and destabilisation of the lithosphere (Rocher et al., 2015; Dahlquist et al., 2024a), leading to partial melting of a heterogeneous continental crust (or continental crust with limited contribution of subcontinental lithospheric mantle), as recorded in Hf-Nd-Sr isotope signatures.

The El Fierro pluton is indicative of an incipient extensional setting within the arc domain, recording the following evolution: (1) initial continental crust melting with the presence of metasediments previously metasomatized during slab retreat (~273 Ma), (2) shallow emplacement (264 Ma) enabled by F-rich compositions that reduced melt viscosity, and (3) transition to incipient rifting. This progression aligns with the model of A-type magmatism acting as a precursor to Triassic breakup, with halogen-rich melts exploiting extensional structures in the thinning lithosphere. Notably, A-type magmatism is commonly reported in areas outside the main magmatic arc, such as foreland or retro-arc regions. This study provides evidence that A-type magmatism can develop within arc settings when specific geodynamic conditions are favourable.

11. Conclusions

New U-Pb zircon data indicate that the El Fierro pluton was emplaced at 262 ± 2 Ma, but zircon antecrysts (~273 Ma) reveal an earlier onset of the late-stage Choiyoi magmatism, overlapping with the waning stages of the early Choiyoi I-type magmatism (285–272 Ma). This suggests a continuous transition from arc-related to extensional magmatism in the Frontal Cordillera of Argentina, revealing also a notable and persistent heat source.

The pluton is ferroan, calc-alkalic to alkali-calcic and predominantly peraluminous with relatively high HFSE and high calculated halogen contents (F up to 31,442 ppm), along with high T_{Zr} and T_{Ap}, confirming its A-type affinity. Geochemical and isotopic data support a hybrid source dominated by metasedimentary crustal material (εHft ≤ −7.0) with minor mantle-derived contributions (εHft up to +1.25).

The studied rocks are highly enriched in F, which would have facilitated shallow emplacement by lowering melt viscosity and solidus temperatures. Furthermore, such fluorine enrichment might reflect primary F-rich sources (e.g., metasomatized continental crust).

The El Fierro pluton records slab retreat and lithospheric thinning during the Permian, transitioning from an extensional arc setting to incipient continental rifting. Its A-type signature underscores the viability of *within-arc* A-type magmatism under appropriate extensional conditions, challenging traditional arc/rift dichotomies.

CRediT authorship contribution statement

Juan A. Moreno: Writing – review & editing, Writing – original draft, Visualization, Methodology, Investigation, Funding acquisition, Data curation, Conceptualization. **Gilmara Santos da Cruz:** Writing – review & editing, Visualization, Investigation. **Juan A. Dahlquist:** Writing – review & editing, Resources, Methodology, Investigation, Funding acquisition, Data curation. **Matías M. Morales Cámera:** Writing – review & editing, Visualization, Investigation. **Priscila S. Zandomeni:** Writing – review & editing, Visualization, Investigation. **Gabriela A. Gonzalez-Liedtke:** Writing – review & editing, Visualization, Investigation. **Miguel A.S. Basei:** Resources, Methodology, Funding acquisition, Formal analysis. **Sanjeet K. Verma:** Writing – review & editing, Visualization, Investigation.

Declaration of competing interest

The authors declare that they have no known competing financial interests or personal relationships that could have appeared to influence the work reported in this paper.

Acknowledgments

The authors acknowledge financial support from: Consejo Nacional de Investigaciones Científicas y Técnicas CONICET [PIP0564], Fondo para la Investigación Científica y Tecnológica FONCyT [PICT 2020 0378 and PICT 2018 1899], Consolidar 2023 SECyT-UNC, and FAPESP [2018/06837-3] linked to Thematic Project FAPESP [2015/03737-0]. Funding for open access charge: Universidad de Huelva / CBUA. We sincerely appreciate the thorough revisions provided by Michael Roden and an anonymous reviewer, which clearly improved the final version of our work. We also thank Editor-in-Chief Astrid Holzheid and the handling editor for their efficient and helpful editorial management.

Appendix A. Supplementary data

Supplementary data to this article can be found online at https://doi.org/10.1016/j.chemer.2026.126388.

References

Azcuy, C.L., Carrizo, H.A., Caminos, R., 1999. Carbonífero y Pérmico de las Sierras Pampeanas, Famatina, Precordillera, Cordillera Frontal y Boque de San Rafael. In: Caminos, R. (Ed.), Geología Argentina, Inst. Geol. Recur. Miner. An, vol. 29, pp. 261–318 (in Spanish).

Bachmann, O., Huber, C., 2019. The inner workings of crustal distillation columns; the physical mechanisms and rates controlling phase separation in silicic magma reservoirs. J. Petrol. 60 (1), 3–18. https://doi.org/10.1093/petrology/egy103.

Bailey, D.K., 1980. Volcanism, earth degassing and replenished lithosphere mantle. Philos. Trans. R. Soc. A Math. Phys. Eng. Sci. 297 (1431), 309–322. https://doi.org/10.1098/rsta.1980.0095.

Bea, F., Fershtater, G., Corretgé, L.G., 1992. The geochemistry of phosphorus in granite rocks and the effect of aluminium. Lithos 29 (1–2), 43–56. https://doi.org/10.1016/0024-4937(92)90027-P.

Bea, F., Montero, P., Molina, J., Scarrow, J., Cambeses, A., Moreno, J., 2018. Lu-Hf ratios of crustal rocks and their bearing on zircon Hf isotope model ages: The effects of accessories. Chem. Geol. 484, 179–190. https://doi.org/10.1016/j.chemgeo.2017.11.034.

Bonin, B., 2007. A-type granites and related rocks: Evolution of a concept, problems and prospects. Lithos 97, 1–29. https://doi.org/10.1016/j.lithos.2006.12.007.

Bouvier, A., Vervoort, J.D., Patchett, P.J., 2008. The Lu–Hf and Sm–Nd isotopic composition of CHUR: Constraints from unequilibrated chondrites and implications for the bulk composition of terrestrial planets. Earth Planet. Sci. Lett. 273, 48–57. https://doi.org/10.1016/j.epsl.2008.06.010.

Breiter, K., Vaňková, M., Vašinová Galiová, M., Korbelová, Z., Kanický, V., 2017. Lithium and trace-element concentrations in trioctahedral micas from granites of different geochemical types measured via laser ablation ICP-MS. Mineral. Mag. 81 (1), 15–33.

Caminos, R.L., 1979. Cordillera Frontal. Segundo Simposio de Geología Regional Argentina. Acad. Nac. Ciencias Córdoba I, 398–453 (Córdoba).

Cardó, R., Díaz, I.N., Cegarra, M., Heredia, N., Rodríguez Fernández, R., Santamaría, G., 2005. Geological Sheet 3169-I, Rodeo, San Juan Province. Instituto de Geología y Recursos Minerales, Servicio Geológico Minero Argentino, 272. Boletín, Buenos Aires, p. 47.

Cardó, R., Díaz, I.N., Limarino, O., Litvak, V., Poma, S., Santamaría, G., 2007. Geological Sheet 2969-III, Malimán, provinces of San Juan and La Rioja, 320. Instituto de Geología y Recursos Minerales, Servicio Geológico Minero Argentino, Boletín, p. 52.

Charoy, B., Raimbault, L., 1994. Zr-, Th-, and REE-rich biotite differentiates in the A-type granite pluton of Suzhou (Eastern China): The key role of fluorine. J. Petrol. 35, 919–962. https://doi.org/10.1093/petrology/35.4.919.

Christiansen, E., Bikun, J.V., Sheridan, M., Burt, D., 1984. Geochemical evolution of topaz rhyolites from the Thomas Range and Spor Mountain. Utah. Am. Mineral. 69, 3–4. https://doi.org/10.2138/am-1984-3-406.

Cobbing, J., 2000. The Geology and Mapping of Granite Batholiths. In: Lecture Notes in Earth Sciences. Springer, Berlin, Heidelberg. https://doi.org/10.1007/3-540-45055-6.

Collins, W.J., Beam, S.D., White, J.R., Chappell, B.W., 1982. Nature and origin of A-type granites with particular reference to south-eastern Australia. Contrib. Mineral. Petrol. 80, 189–200. https://doi.org/10.1007/BF00375438.

Dahlquist, J.A., Alasino, P.H., Eby, G.N., Galindo, C., Casquet, C., 2010. Fault controlled Carboniferous A-type magmatism in the proto-Andean foreland (Sierras Pampeanas, Argentina): Geochemical constraints and petrogenesis. Lithos 115, 65–81. https://doi.org/10.1016/j.lithos.2009.11.006.

Dahlquist, J.A., Alasino, P.H., Basei, M.A.S., Morales Camera, M., Macchioli Grande, M., da Costa Campos Neto, M.C., 2018. Petrological, geochemical, isotopic, and geochronological constraints for the Late Devonian–early Carboniferous magmatism in SW Gondwana (27°–32° LS): an example of geodynamic switching. Int. J. Earth Sci. 107, 2575–2603. https://doi.org/10.1007/s00531-018-1645-2.

Dahlquist, J.A., Morales Cámera, M.M., Alasino, P.H., Pankhurst, R.J., Basei, M.A.S., Rapela, C.W., Moreno, J.A., Baldo, E.G., Galindo, C., 2021. A review of Devonian–Carboniferous magmatism in the central region of Argentina, pre-Andean margin of SW Gondwana. Earth Sci. Rev. 221, 103781. https://doi.org/10.1016/j.earscirev.2021.103781.

Dahlquist, J.A., Morales Cámera, M.M., Moreno, J.A., Basei, M.A.S., Zandomeni, P., Santos da Cruz, G., 2023. Integrated U-Pb and Hf zircon and whole-rock Nd isotopes studies of Devonian granitic rocks from Sierra de San Luis (Sierras Pampeanas, Argentina): Petrogenetic implications. Andean Geol. 50 (2), 167–180. https://doi.org/10.5027/andgeoV50n2-3639.

Dahlquist, J.A., Morales Cámera, M.M., Santos da Cruz, G., Basei, M.A.S., Moreno, J.A., Rocher, S., Tickyj, H., Passarelli, C.R., 2024a. Generation and evolution of the Choiyoi granitic magmatism based on U-Pb zircon studies, Cordón del Portillo, Frontal Cordillera (Argentina). J. S. Am. Earth Sci. 147, 105134. https://doi.org/10.1016/j.jsames.2024.105134.

Dahlquist, J.A., Morales Cámera, M.M., Moreno, J.A., Tickyj, H., Basei, M.A.S., Santos da Cruz, G., Rocher, S., 2024b. Evolution of Devonian and Carboniferous pre-Andean arc magmatism in the Frontal Cordillera (27°–35°S), Argentina: Insights from U–Pb zircon and isotopic studies. J. S. Am. Earth Sci. 143, 105015. https://doi.org/10.1016/j.jsames.2024.105015.

Dahlquist, J.A., Morales Cámera, M.M., Moreno, J.A., Basei, M.A.S., Santos da Cruz, G., Oliveira, E.P., 2024c. A conceptual model for the evolution of a magmatic system based on U-Pb zircon studies on the Devonian granites of Sierra de San Luis. Argentina. Int. Geol. Rev. 66 (9), 1794–1814. https://doi.org/10.1080/00206814.2024.2335676.

Dahlquist, J.A., Morales Cámera, M.M., Moreno, J.A., Basei, M.A.S., Santos da Cruz, G., 2025. Lu-Hf zircon isotopes data from Devonian granitic rocks of Sierra de San Luis, Argentina: Petrogenetic implications combining previous U-Pb and Hf zircon data. Int. Geol. Rev. 1–15. https://doi.org/10.1080/00206814.2025.2527817.

Dall'Agnol, R., Oliveira, D.C., 2007. Oxidized, magnetite-series, rapakivi-type granites of Carajás, Brazil: Implications for classification and petrogenesis of A-type granites. Lithos 93 (3–4), 215–233. https://doi.org/10.1016/j.lithos.2006.03.065.

Dall'Agnol, R., Cunha, I.R.V., Guimarães, F.V., Oliveira, D.C., Teixeira, M.F.B., Feio, G.R.L., Lamarão, C.N., 2017. Mineralogy, geochemistry, and petrology of Neoarchean ferroan to magnesian granites of Carajás Province, Amazonian Craton: The origin of hydrated granites associated with charnockites. Lithos 277, 3–32. https://doi.org/10.1016/j.lithos.2016.09.032.

Debon, F., Le Fort, P., 1983. A chemical–mineralogical classification of common plutonic rocks and associations. Earth Environ. Sci. Trans. R. Soc. Edinburgh 73 (3), 135–149. https://doi.org/10.1017/S0263593300010117.

del Rey, A., Deckart, K., Arriagada, C., Martínez, F., 2016. Resolving the paradigm of the late Paleozoic–Triassic Chilean magmatism: Isotopic approach. Gondwana Res. 7, 172–181. https://doi.org/10.1016/j.gr.2016.06.008.

DePaolo, D.J., Linn, A.M., Schubert, G., 1991. The continental crustal age distribution: Methods of determining mantle separation ages from Sm-Nd isotopic data and application to the southwestern United States. J. Geophys. Res. Solid Earth 96 (B2), 2071–2088. https://doi.org/10.1029/90JB02219.

Eby, G.N., 1990. The A-type granitoids: A review of their occurrence and chemical characteristics and speculations on their petrogenesis. Lithos 26, 115–134. https://doi.org/10.1016/0024-4937(90)90043-Z.

Eby, G.N., 1992. Chemical subdivision of the A-type granitoids: Petrogenetic and tectonic implications. Geology 20 (7), 641–644. https://doi.org/10.1130/0091-7613(1992)020<0641:CSOTAT>2.3.CO;2.

Frost, B.R., Barnes, C.G., Collins, W.J., Arculus, R.J., Ellis, D.J., Frost, C.D., 2001. A geochemical classification for granitic rocks. J. Petrol. 42, 2033–2048. https://doi.org/10.1093/petrology/42.11.2033.

Gao, P., Zheng, Y.F., Zhao, Z.F., 2017. Triassic granites in South China: a geochemical perspective on their characteristics, petrogenesis, and tectonic significance. Earth Sci. Rev. 173, 266–294. https://doi.org/10.1016/j.earscirev.2017.07.016.

Gianni, G.M., Navarrete, C.R., 2022. Catastrophic slab loss in southwestern Pangea preserved in the mantle and igneous record. Nat. Commun. 13, 698. https://doi.org/10.1038/s41467-022-28116-5.

Glazner, A., Bartley, J., Coleman, D., Gray, W., Taylor, R.Z., 2004. Are plutons assembled over millions of years by amalgamation from small magma chambers? GSA Today 14, 4–11. https://doi.org/10.1130/1052-5173(2004)014<0004:APAOMO>2.0.CO;2.

Glazner, A.F., Bartley, J.M., Coleman, D.S., Lindgren, K., 2020. Aplite diking and. infiltration: a differentiation mechanism restricted to plutonic rocks. Contrib. Mineral. Petrol. 175 (4), 1–17. https://doi.org/10.1007/s00410-020-01677-1.

Gregori, D.A., Martínez, J.C., Benedini, L., 2013. The Gondwana–South America Iapetus margin evolution as recorded by Lower Paleozoic units of western Precordillera, Argentina: The Bonilla Complex. Uspallata. Serie Correlación Geol. 29 (1), 21–80.

Griffin, W.L., Wang, X., Jackson, S.E., Pearson, N.J., O'Reilly, S.Y., 2002. Zircon geochemistry and magma mixing, SE China: in-situ analysis of Hf isotopes, Tonglu and Pingtan igneous complexes. Lithos 61, 237–269. https://doi.org/10.1016/S0024-4937(02)00082-8.

Griffin, W.L., Belousova, E.A., Shee, S.R., Pearson, N.J., O'Reilly, S.Y., 2004. Archean. crust evolution in the northern Yilgarn Craton: U-Pb and Hf-isotope evidence from detrital zircons. Precambrian Res. 131, 231–282.

Groeber, P., 1951. La Alta Cordillera entre las latitudes 34° y 29°30′. Inst. Investig. Cienc. Nat., Rev. Mus. Argent. Cienc. Nat. Bernardino Rivadavia, Ciencias Geol. 1, 1–352 (in Spanish).

Harrison, T.M., Watson, E.B., 1984. The behavior of apatite during crustal anatexis: equilibrium and kinetic considerations. Geochim. Cosmochim. Acta 48, 1467–1477. https://doi.org/10.1016/0016-7037(84)90215-5.

Jenkin, G.R.T., Ellam, R.M., Rogers, G., Stuart, F.M., 2001. An investigation of closure temperature of the biotite Rb–Sr system: The importance of cation exchange. Geochim. Cosmochim. Acta 65 (7), 1141–1158. https://doi.org/10.1016/S0016-7037(00)00558-4.

Jones, R.E., Kirstein, L.A., Kasemann, S.A., Dhuime, B., Elliott, T., Litvak, V.D., Alonso, R., Hinton, R., Facility, E.I.M., 2015. Geodynamic controls on the contamination of Cenozoic arc magmas in the southern Central Andes: insights from the O and Hf isotopic composition of zircon. Geochim. Cosmochim. Acta 164, 386–402. https://doi.org/10.1016/j.gca.2015.05.029.

Kay, S.M., Ramos, V.A., Mpodozis, C., Sruoga, P., 1989. Late Paleozoic to Jurassic silicic magmatism at the Gondwana margin: Analogy to middle Proterozoic in North America? Geology 17, 324–328. https://doi.org/10.1130/0091-7613(1989)017<0324:LPTJSM>2.3.CO;2.

Kemp, A.I.S., Hawkesworth, C.J., Foster, G.L., Paterson, G.A., Woodhead, J.D., Hergt, J.M., Gray, C.M., Whitehouse, M.J., 2007. Magmatic and crustal differentiation history of granitic rocks from Hf–O isotopes in zircon. Science 315 (5814), 980–983. https://doi.org/10.1126/science.1136154.

Keppler, H., 1993. Influence of fluorine on the enrichment of high field strength trace elements in granitic rocks. Contrib. Mineral. Petrol. 114, 479–488.

King, P.L., Chappell, B.W., Allen, C.M., White, A.J.R., 2001. Are A-type granites the high temperature. felsic granites? Evidence from fractionated granites of the Wangrah Suite. Aust. J. Earth Sci. 48, 501–514.

Landenberger, B., Collins, W.J., 1996. Derivation of A-type granites from a dehydrated charnockitic lower crust: Evidence from the Chaelundi complex, eastern Australia. J. Petrol. 37, 145–170.

Laurent, O., Rapoport, M., Stevens, G., Moyen, J.F., Martin, H., Doucelance, R., Bosq, C., 2014. Contrasting petrogenesis of Mg-K and Fe-K granitoids and implications for postcollisional magmatism: Case study from the Late-Archean Matok pluton (Pietersburg block, South Africa). Lithos 196–197, 131–149. https://doi.org/10.1016/j.lithos.2014.01.006.

Li, X., Zhang, C., Wang, L., Behrens, H., Holtz, F., 2020. Experiments on the saturation of fluorite in magmatic systems: Implications for maximum F concentration and fluorine–cation bonding in silicate melt. J. Earth Sci. 31 (3), 456–467. https://doi.org/10.1007/s12583-020-1304-0.

Lim, H., Nebel, O., Weinberg, R.F., Nebel-Jacobsen, Y., Barrote, V.R., Park, J., Myeong, B., Cawood, P.A., 2023. Lower crustal hot zones as zircon incubators? Inherited zircon antecrysts in diorites from a mafic mush reservoir. In: van Schijndel, V., Cutts, K., Pereira, I., Guitreau, M., Volante, S., Tedeschi, M. (Eds.), Minor Minerals, Major Implications: Using Key Mineral Phases to Unravel the Formation and Evolution of Earth's Crust, 537. Geol. Soc. Lond. Spec. Publ, pp. 411–433. https://doi.org/10.1144/SP537-2021-195.

Llambías, E.J., Sato, A.M., 1990. El batolito de Colangüil (29–31°S) Cordillera Frontal de Argentina: Estructura y marco tectónico. Rev. Geol. Chile 17 (1), 89–108 (in Spanish).

Llambías, E.J., Sato, A.M., 1995. El batolito de Colangüil: Transición entre orogénesis y anorogénesis. Rev. Asoc. Geol. Argent. 50 (1–4), 111–131 (in Spanish).

London, D., 1997. Estimating abundances of volatile and other mobile components in evolved silicic melts through mineral–melt equilibria. J. Petrol. 38, 1691–1706. https://doi.org/10.1093/petrology/38.12.1691.

London, D., 2008. Pegmatites. Canadian Mineralogist Special. Publication 10, 368.

Martin, R.F., 2006. A-type granites of crustal origin ultimately result from open-system fenitization-type reactions in an extensional environment. Lithos 91, 125–136. https://doi.org/10.1016/j.lithos.2006.03.012.

McDonough, W.F., Sun, S.S., 1995. The composition of the Earth. Chem. Geol. 120, 223–253. https://doi.org/10.1016/0009-2541(94)00140-4.

Miller, C.F., Stoddard, E.F., Bradfish, L.J., Dollase, W.A., 1981. Composition of plutonic muscovite: genetic implications. Can. Mineral. 19, 25–34.

Montero, P., Bea, F., Corretge, L.G., Floor, P., Whitehouse, M.J., 2009. U–Pb ion microprobe dating and Sr–Nd isotope geology of the Galiñeiro Intrusive Complex. Lithos 107, 227–238. https://doi.org/10.1016/j.lithos.2008.11.004.

Morales Cámera, M.M., Dahlquist, J.A., García-Arias, M., Moreno, J.A., Galindo, C., Basei, M.A.S., Molina, J.F., 2020. Petrogenesis of the F-rich peraluminous A-type granites: An example from the Devonian Achala batholith (Characato Suite), Sierras Pampeanas. Argentina. Lithos 378–379, 105792. https://doi.org/10.1016/j.lithos.2020.105792.

Morales Cámera, M.M., Dahlquist, J.A., Moreno, J.A., Zandomeni, P.S., García-Arias, M., Basei, M.A.S., 2022. The Andaluca plutonic unit, Vinquis Intrusive Complex, Argentina: An assessment of mantle role in the genesis of Early Carboniferous weakly peraluminous A-type granites in the pre-Andean SW Gondwana margin. Lithos 434–435, 106873. https://doi.org/10.1016/j.lithos.2022.106873.

Moreno, J.A., Molina, J.F., Montero, P., Abu Anbar, M., Scarrow, J.H., Cambeses, A., Bea, F., 2014. Unraveling sources of A-type magmas in juvenile continental crust: Constraints from compositionally diverse Ediacaran post-collisional granitoids in the Katerina Ring Complex, southern Sinai. Egypt. Lithos 192–195, 56–85. https://doi.org/10.1016/j.lithos.2014.01.010.

Moreno, J.A., Molina, J.F., Bea, F., Abu Anbar, M., Montero, P., 2016. Th–REE- and Nb–Ta-accessory minerals in post-collisional Ediacaran felsic rocks from the Katerina Ring Complex (S. Sinai, Egypt): An assessment for the fractionation of Y/Nb, Th/Nb, La/Nb and Ce/Pb in highly evolved A-type granites. Lithos 258–259, 173–196. https://doi.org/10.1016/j.lithos.2016.04.020.

Moreno, J.A., Baldim, M.R., Semprich, J., Oliveira, E.P., Verma, S.K., Teixeira, W., 2017. Geochronological and geochemical evidences for extension-related Neoarchean granitoids in the southern São Francisco Craton. Brazil. Precambrian Res. 294, 322–343. https://doi.org/10.1016/j.precamres.2017.04.011.

Moreno, J.A., Dahlquist, J.A., Morales Cámera, M.M., Alasino, P.H., Larrovere, M.A., Basei, M.A.S., Galindo, C., Zandomeni, P.S., Roche, S., 2020. Geochronology and geochemistry of the Tabaquito batholith (Frontal Cordillera, Argentina): Geodynamic implications and temporal correlations in the SW Gondwana margin. J. Geol. Soc. Lond. 177, 455–474. https://doi.org/10.1144/jgs2019-062.

Muñoz, J.L., 1984. F-OH and Cl-OH exchange in micas with applications to hydrothermal ore deposits. In: Bailey, S.W. (Ed.), Reviews in Mineralogy, Micas, vol. 13. Mineralogical Society of America, pp. 469–493.

Muñoz, J.L., 1992. Calculation of HF and HCl fugacities from biotite compositions: Revised equations. Geol. Soc. Am. Abstr. Programs 24, A221.

Nachit, H., Ibhi, A., Abia, E.H., Ben Ohoud, M., 2005. Discrimination between primary magmatic biotites, reequilibrated biotites and neoformed biotites. Compt. Rendus Geosci. 337, 1415–1420. https://doi.org/10.1016/j.crte.2005.08.006.

Oliveros, V., Vásquez, P., Creixell, C., Lucassen, F., Ducea, M.N., Ciocca, I., González, J., Espinoza, M., Salazar, E., Coloma, F., Kasemann, S.A., 2020. Lithospheric evolution of the pre- and early Andean convergent margin. Chile. Gondwana Res. 80, 202–227. https://doi.org/10.1016/j.gr.2019.11.002.

Poole, G.H., Kemp, A.I.S., Hagemann, S.G., Fiorentini, M.L., Jeon, H., Williams, I.S., Zappettini, E.O., Rubinstein, N.A., 2020. The petrogenesis of back-arc magmas, constrained by zircon O and Hf isotopes, in the Frontal Cordillera and Precordillera. Argentina. Contrib. Mineral. Petrol. 175, 89. https://doi.org/10.1007/s00410-020-1717-7.

Quartino, B.J., Zardini, R.A., 1967. Geología y petrología de la Cordillera de Colangüil y las serranías de Santa Rosa y San Guillermo, Cordillera Frontal de San Juan. Rev. Asoc. Geol. Argent. 22, 5–63 (in Spanish).

Rocher, A., Vallecillo, G.M., de Machuca, C., Alasino, B., 2015. El Grupo Choiyoi (Pérmico temprano–medio) en la Cordillera Frontal de Calingasta, San Juan, Argentina: Volcanismo de arco asociado a extensión. Rev. Mex. Cienc. Geol. 32, 415–432 (in Spanish).

Rocher, S., Alasino, P.H., Dahlquist, J.A., Basei, M.A.S., 2024. Permian–Triassic volcanic and plutonic records of the Argentine Frontal Cordillera: A review with new U–Pb and Hf-isotope zircon data. J. S. Am. Earth Sci. 149, 105181. https://doi.org/10.1016/j.jsames.2024.105181.

Rowe, M.C., Wolff, J.A., Gardner, J.N., Ramos, F.C., Teasdale, R., Heikoop, C.E., 2007. Development of a continental volcanic field: petrogenesis of pre-caldera intermediate and silicic rocks and origin of the Bandelier magmas, Jemez Mountains (New Mexico, USA). J. Petrol. 48, 2063–2091.

Sallet, R., 2000. Fluorine as a tool in the petrogenesis of quartz-bearing magmatic associations: Applications of an improved F–OH biotite–apatite thermometer grid. Lithos 50, 241–253. https://doi.org/10.1016/S0024-4937(99)00036-5.

Santos da Cruz, G., Moreno, J.A., Dahlquist, J.A., Morales Cámera, M.M., Basei, M.A.S., Zandomeni, P.S., 2024. Contributing to understand how Cordilleran batholiths build from detailed geochronology of the Carboniferous Tabaquito batholith, Frontal Cordillera (Argentina). In: Molina, J.F., Cambeses, A., García Casco, A., Montero, P. (Eds.), F. Bea's Work Celebration, 662. Chem. Geol, 122245. https://doi.org/10.1016/j.chemgeo.2024.122245.

Sato, A.M., Kawashita, K., 1988. Edad Rb-Sr de la última intrusión del Batolito de Colangüil, provincia de San Juan. Rev. Asoc. Geol. Argent. 43, 415–418.

Sato, A.M., Llambías, E., Basei, M., Castro, E., 2015. Three stages in the late Paleozoic to Triassic magmatism of southwestern Gondwana, and the relationships with the volcanogenic events in coeval basins. J. S. Am. Earth Sci. 63, 48–69. https://doi.org/10.1016/j.jsames.2015.07.005.

Skjerlie, K.P., Johnston, A.D., 1993. Fluid-absent melting behavior of an F-rich tonalitic gneiss at mid-crustal pressures: Implications for the generation of anorogenic granites. J. Petrol. 34 (4), 785–815. https://doi.org/10.1093/petrology/34.4.785.

Söderlund, U., Patchett, J.P., Vervoort, J.D., Isachsen, C.E., 2004. The ^{176}Lu decay constant determined by Lu–Hf and U–Pb isotope systematics of Precambrian mafic intrusions. Earth Planet. Sci. Lett. 219, 311–324. https://doi.org/10.1016/S0012-821X(04)00012-3.

Stern, R.J., 2002. Crustal evolution in the East African Orogen: A neodymium isotopic perspective. J. Afr. Earth Sci. 34 (3–4), 109–117. https://doi.org/10.1016/S0899-5362(02)00012-X.

Sylvester, P.J., 1989. Post-collisional alkaline granites. J. Geol. 97, 261–280. https://doi.org/10.1086/629127.

Teixeira, R.J.S., Neiva, A.M.R., Silva, P.B., Gomes, M.E.P., Andersen, T., Ramos, J.M.F., 2011. Combined U–Pb geochronology and Lu–Hf isotope systematics by LAM–ICPMS of zircons from granites and metasedimentary rocks of Carrazeda de Ansiães and Sabugal areas, Portugal, to constrain granite sources. Lithos 125 (1–2), 321–334. https://doi.org/10.1016/j.lithos.2011.02.015.

Tischendorf, G., Rieder, M., Förster, H.-J., Gottesmann, B., Guidotti, C.V., 2004. A new graphical presentation and subdivision of potassium micas. Mineral. Mag. 68, 649–667. https://doi.org/10.1180/0026461046840210.

Tischendorf, G., Förster, H.-J., Gottesmann, B., Rieder, M., 2007. True and brittle micas: Composition and solid-solution series. Mineral. Mag. 71, 285–320. https://doi.org/10.1180/minmag.2007.071.1.285.

Verma, S.P., Pandarinath, K., Verma, S.K., Agrawal, S., 2013. Fifteen new discriminant-function-based multi-dimensional robust diagrams for acid rocks and their application to Precambrian rocks. Lithos 168, 113–123. https://doi.org/10.1016/j.lithos.2013.05.002.

Vervoort, J.D., Kemp, A.I.S., 2016. Clarifying the zircon Hf isotope record of crust–mantle evolution. Chem. Geol. 425, 65–75. https://doi.org/10.1016/j.chemgeo.2016.01.023.

Villaseca, C., Barbero, L., Herreros, V., 1998. A re-examination of the typology of peraluminous granite types in intracontinental orogenic belts. Earth Environ. Sci. Trans. R. Soc. Edinb. 89 (2), 113–119. https://doi.org/10.1017/S0263593300007045.

Wang, L.-X., Ma, C.-Q., Zhang, C., Zhu, Y.-X., Marks, M.A.W., 2018. Halogen geochemistry of I- and A-type granites from Jiuhuashan region (South China): Insights into the elevated fluorine in A-type granite. Chem. Geol. 478, 164–182. https://doi.org/10.1016/j.chemgeo.2017.09.033.

Watson, E.B., Harrison, T.M., 1983. Zircon saturation revisited: Temperature and composition effects in a variety of crustal magma types. Earth Planet. Sci. Lett. 64, 295–304. https://doi.org/10.1016/0012-821X(83)90211-X.

Webster, J.D., 1997. Exsolution of magmatic volatile phases from Cl-enriched mineralizing granitic magmas and implications for ore metal transport. Geochim. Cosmochim. Acta 61, 1017–1029.

Webster, J.D., Tappen, C.M., Mandeville, C.W., 2009. Partitioning behavior of chlorine. and fluorine in the system apatite–melt–fluid. II: felsic silicate systems at 200 MPa. Geochim. Cosmochim. Acta 73, 559–581.

Whalen, J.B., Currie, K.L., Chappell, B.W., 1987. A-type granites: Geochemical characteristics, discrimination and petrogenesis. Contrib. Mineral. Petrol. 95 (4), 407–419. https://doi.org/10.1007/BF00402202.

Whitney, J.A., 1988. The origin of granite: The role and source of water in the evolution of granitic magmas. Geol. Soc. Am. Bull. 100, 1886–1897. https://doi.org/10.1130/0016-7606(1988)100<1886:TOOGTR>2.3.CO;2.

Whitney, D.L., Evans, B.W., 2010. Abbreviations for names of rock-forming minerals. Am. Mineral. 95, 185–187. https://doi.org/10.2138/am.2010.3371.

Yang, J.-H., Wu, F.-Y., Wilde, S.A., Xie, L.-W., Yang, Y.-H., Liu, X.-M., 2007. Tracing magma mixing in granite melt–peridotite interactions in the Trans-North China Orogen: U–Pb dating, Hf isotopes and trace elements in zircons from mantle xenoliths. J. Petrol. 51, 537–571. https://doi.org/10.1093/petrology/egp088.

Zandomeni, P.S., Verdecchia, S.O., Baldo, E.G., Galindo, C., Moreno, J.A., Dahlquist, J.A., Casquet, C., Morales Cámera, M.M., Basei, M.A.S., Ramacciotti, C.D., 2021. Early Ordovician magmatism in the Sierra de Ancaján, Sierras Pampeanas (Argentina): implications for the early evolution of the proto-Andean margin of Gondwana. J. Iber. Geol. 47, 39–63.